

## Supplementary Materials for

### **Dissecting the multicellular ecosystem of metastatic melanoma by single-cell RNA-seq**

Itay Tirosh, Benjamin Izar,\* Sanjay M. Prakadan, Marc H. Wadsworth II, Daniel Treacy, John J. Trombetta, Asaf Rotem, Christopher Rodman, Christine Lian, George Murphy, Mohammad Fallahi-Sichani, Ken Dutton-Regester, Jia-Ren Lin, Ofir Cohen, Parin Shah, Diana Lu, Alex S. Genshaft, Travis K. Hughes, Carly G. K. Ziegler, Samuel W. Kazer, Aleth Gaillard, Kellie E. Kolb, Alexandra-Chloé Villani, Cory M. Johannessen, Aleksandr Y. Andreev, Eliezer M. Van Allen, Monica Bertagnolli, Peter K. Sorger, Ryan J. Sullivan, Keith T. Flaherty, Dennie T. Frederick, Judit Jané-Valbuena, Charles H. Yoon, Orit Rozenblatt-Rosen, Alex K. Shalek, Aviv Regev,\* Levi A. Garraway\*

\*Corresponding author. E-mail: [bizar@partners.org](mailto:bizar@partners.org) (B.I.); [aregev@broadinstitute.org](mailto:aregev@broadinstitute.org) (A.R.); [levi\\_garraway@dfci.harvard.edu](mailto:levi_garraway@dfci.harvard.edu) (L.A.G.)

Published 8 April 2016, *Science* **352**, 189 (2016)  
DOI: 10.1126/science.aad0501

#### This PDF file includes:

Materials and Methods  
Figs. S1 to S24  
Tables S1, S10, and S11  
Full Reference List

#### Other Supplementary Material for this manuscript includes the following: (available at [www.sciencemag.org/content/352/6282/189/suppl/DC1](http://www.sciencemag.org/content/352/6282/189/suppl/DC1))

Tables S2 to S9 and S12 to S16 (Excel files)

# **Dissecting the multicellular ecosystem of metastatic melanoma by single-cell RNA-seq**

## **Materials and Methods**

### **Tissue handling and tumor disaggregation.**

Resected tumors were transported in DMEM (ThermoFisher Scientific, Waltham, MA) on ice immediately after surgical procurement. Tumors were rinsed with PBS (Life Technologies, Carlsbad, CA). A small fragment was stored in RNA-protect (Qiagen, Hilden, Germany) for bulk RNA and DNA isolation. Using scalpels, the remainder of the tumor was minced into tiny cubes <1 mm<sup>3</sup> and transferred into a 50 ml conical tube (BD Falcon, Franklin Lakes, NJ) containing 10 ml pre-warmed M199-media (ThermoFisher Scientific), 2 mg/ml collagenase P (Roche, Basel, Switzerland) and 10U/μl DNase I (Roche). Tumor pieces were digested in this digestion media for 10 minutes at 37°C, then vortexed for 10 seconds and pipetted up and down for 1 minute using pipettes of descending sizes (25 ml, 10 ml and 5 ml). If needed, this was repeated twice more until a single-cell suspension was obtained. This suspension was then filtered using a 70μm nylon mesh (ThermoFisher Scientific) and residual cell clumps were discarded. The suspension was supplemented with 30 ml PBS (Life Technologies) with 2% fetal calf serum (FCS) (Gemini Bioproducts, West Sacramento, CA) and immediately placed on ice. After centrifuging at 580g at 4°C for 6 minutes, the supernatant was discarded and the cell pellet was re-suspended in PBS with FCS and placed on ice prior to staining for FACS.

### **FACS.**

Single-cell suspensions were stained with CD45-FITC (VWR, Radnor, PA) and Calcein-AM (Life Technologies) per manufacturer recommendations. For sorting of *ex vivo* co-cultured cancer-associated fibroblasts, we used a CD90-PE antibody (BioLegend, San Diego, CA). First,

doublets were excluded based on forward and sideward scatter, then we gated on viable cells (*Calcein*<sup>high</sup>) and sorted single cells (CD45+ or CD45- or CD45-CD90+) into 96-well plates chilled to 4°C, pre-prepared with 10µl TCL buffer (Qiagen) supplemented with 1% beta-mercaptoethanol (lysis buffer). Single-cell lysates were sealed, vortexed, spun down at 3700 rpm at 4°C for 2 minutes, immediately placed on dry ice and transferred for storage at -80°C.

### **RNA and DNA isolation from bulk specimens.**

RNA and DNA were isolated using the Qiagen minikit following the manufacturers recommendations.

### **Whole transcriptome amplification.**

Whole Transcriptome amplification (WTA) was performed with a modified SMART-Seq2 protocol, as described previously (51, 52), with Maxima Reverse Transcriptase (Life Technologies) used in place of Superscript II.

### **Library preparation and RNA-seq.**

WTA products were cleaned with Agencourt XP DNA beads and 70% ethanol (Beckman Coulter, Brea, CA) and Illumina sequencing libraries were prepared using Nextera XT (Illumina, San Diego, CA), as previously described (52). The 96 samples of a multiwall plate were pooled together, and cleaned with two 0.8x DNA SPRIIs (Beckman Coulter). Library quality was assessed with a high sensitivity DNA chip (Agilent) and quantified with a high sensitivity dsDNA Quant Kit (Life Technologies). Samples were sequenced on an Illumina NextSeq 500 instrument using 30bp paired-end reads.

**Whole-exome sequencing and analysis.** Exome sequences were captured using Illumina technology and Exome sequence data processing and analysis were performed using the Picard and Firehose pipelines at the Broad Institute. The Picard pipeline (<http://picard.sourceforge.net>) was used to produce a BAM file with aligned reads. This includes alignment to the hg19 human reference sequence using the Burrows-Wheeler transform algorithm (53) and estimation of base quality score and recalibration with the Genome Analysis Toolkit (GATK) (<http://www.broadinstitute.org/gatk/>) (54). All sample pairs passed the Firehose pipeline including a QC pipeline to test for any tumor/normal and inter-individual contamination as previously described (55, 56). The MuTect algorithm was used to identify somatic mutations (56). MuTect identifies candidate somatic mutations by Bayesian statistical analysis of bases and their qualities in the tumor and normal BAMs at a given genomic locus. To reduce false positive calls we additionally analyzed reads covering sites of an identified somatic mutation and realigned them with NovoAlign ([www.novocraft.com](http://www.novocraft.com)) and performed additional iteration of MuTect inference on newly aligned BAM files. Furthermore, we filtered somatic mutation calls using a panel of over 8,000 TCGA Normal samples. Small somatic insertions and deletions were detected using the Strelka algorithm (57) and similarly subjected to filtering out potential false positive using the panel of TCGA Normal samples. Somatic mutations including single-nucleotide variants, insertions, and deletions were annotated using Oncotator (58). Copy-ratios for each captured exon were calculated by comparing the mean exon coverage with expected coverage based on a panel of normal samples. The resulting copy-ratio profiles were then segmented using the circular binary segmentation (CBS) algorithm(59).

## Processing of RNA-seq data

Following sequencing on the NextSeq, BAM files were converted to merged, demultiplexed FASTQs. Paired-end reads were then mapped to the UCSC hg19 human transcriptome using Bowtie (60) with parameters "-q --phred33-quals -n 1 -e 99999999 -l 25 -I 1 -X 2000 -a -m 15 -S -p 6", which allows alignment of sequences with single base changes such as due to point mutations. Expression levels of genes were quantified as  $E_{i,j} = \log_2(TPM_{i,j}/10+1)$ , where  $TPM_{i,j}$  refers to transcript-per-million (TPM) for gene  $i$  in sample  $j$ , as calculated by RSEM (61) v1.2.3 in paired-end mode. TPM values were divided by 10 since we estimate the complexity of our single cell libraries to be on the order of 100,000 transcripts and would like to avoid counting each transcript ~10 times, as would be the case with TPM, which may inflate the difference between the expression level of a gene in cells in which the gene is detected and those in which it is not detected. When evaluating the average expression of a population of cells by pooling data across cells (e.g., all cells from a given tumor or cell type) the division by 10 was not required and the average expression was defined  $E_p(I) = \log_2(TPM(I)+1)$ , where  $I$  is a set of cells.

For each cell, we quantified the number of genes for which at least one read was mapped, and the average expression level of a curated list of housekeeping genes (Table S16). We then excluded all cells with either fewer than 1,700 detected genes or an average housekeeping expression ( $E$ , as defined above) below 3. For the remaining cells, we calculated the pooled expression of each gene as ( $E_p$ ), and excluded genes with an aggregate expression below 4, which defined a different set of genes in different analyses depending on the subset of cells included. For the remaining cells and genes, we defined relative expression by centering the expression levels,  $E_{r,i,j} = E_{i,j} - \text{average}[E_{i,1\dots n}]$ .

## CNV estimation

Initial CNVs ( $CNV_0$ ) were estimated by sorting the analyzed genes by their chromosomal location and applying a moving average to the relative expression values, with a sliding window of 100 genes within each chromosome, as previously described (15). To avoid considerable impact of any particular gene on the moving average we limited the relative expression values to [-3,3] by replacing all values above 3 by 3, and replacing values below -3 by -3. This was performed only in the context of CNV estimation. This initial analysis is based on the average expression of genes in each cell compared to all other cells and therefore does not have a proper reference which is required to define the baseline. However, we identified five subsets of cells that each had more limited high or low values of  $CNV_0$  and which were consistent across the genome despite the fact that these cells originate from multiple tumors. We thus considered these as putative non-malignant cells and used their CNV estimates to define the baseline. The normal cells included five cell types (see below, not including NK cells), which differed in gene expression patterns and accordingly also slightly in CNV estimates (*e.g.*, the MHC region in chromosome 6 had consistently higher values in T cells than in stromal or cancer cells). We therefore defined multiple baselines, as the average of each cell type, and based on these the maximal ( $BaseMax$ ) and minimal ( $BaseMin$ ) baseline at each window of 100 genes. The final CNV estimate of cell  $i$  at position  $j$  was then defined as:

$$CNV_f(i,j) = \begin{cases} CNV_0(i,j) - BaseMax(j), & \text{if } CNV_0(i,j) > BaseMax(j) + 0.2 \\ CNV_0(i,j) - BaseMin(j), & \text{if } CNV_0(i,j) < BaseMin(j) - 0.2 \\ 0, & \text{if } BaseMin(j) - 0.2 < CNV_0(i,j) < BaseMin(j) + 0.2 \end{cases}$$

To quantitatively evaluate how likely each cell is to be a malignant or non-malignant cell we summarized the CNV pattern of each cell by two values: (1) overall CNV signal, defined as the sum of squares of the  $CNV_f$  estimates across all windows; (2) the correlation of each cells'  $CNV_f$  vector with the average  $CNV_f$  vector of the top 10% of cells from the same tumor with respect to CNV signal (*i.e.*, the most confidently-assigned malignant cells). These two values

were used to classify cells as malignant, non-malignant, and intermediates that were excluded from further analysis, as shown in **Fig. S1B**.

### T-SNE analysis and cell type classification

A Matlab implementation of the tSNE method was downloaded from <http://lvdmaaten.github.io/tsne/> and applied with dim=15 to the relative expression data of malignant and to that of non-malignant cells. Since the complexity of tSNE visualization increases with the number of tumors we restricted the analysis presented in Fig. 1 to the 13 tumors with at least 100 cells, and for the malignant cell analysis we further restricted the analysis to 6 tumors with >50 malignant cells. To define cell types from the non-malignant tSNE analysis we used a density clustering method, DBscan (19). This process revealed six clusters for which the top preferentially expressed genes ( $p<0.001$ , permutation test) included multiple known markers of particular cell types. In this way, we identified T cell, B-cell, macrophage, endothelial, CAF (cancer-associated fibroblast) and NK cell clusters, as marked in Fig. 1D (dashed ellipses). To ensure the specificity of our assignment of individual cells to each cell type cluster, while avoiding potential doublet cells (which might be composed of two cells from distinct cell types), cells with low-quality data, and cells that spuriously cluster with a certain cell type, we next scored each non-malignant cell (by CNV estimates, as described above) by the average expression of the identified cell type marker genes. Cells were classified as each cell type only if they express the marker genes for that cell type much more than those for any other cell type (average relative expression,  $E_r$ , of markers for one cell type higher by at least 3 than those of other cell types, which corresponds to 8-fold expression difference). A full list of the genes preferentially expressed in each cell type as well as the subset that were used as marker genes is given in Table S3.

## **Principal component analysis**

In order to decrease the impact of inter-tumoral variability on the combined analysis of cancer cells we re-centered the data within each tumor separately, such that the average of each gene was zero among cells from each tumor. The covariance matrix used for PCA was generated using an approach outlined in Shalek et al. (62) to decrease the weight of less reliable “missing” values in the data. This approach aims to address the challenge that arises due to the limited sensitivity of single-cell RNA-seq, where many genes are not detected in a particular cell despite being expressed. This is particularly pronounced for genes that are more lowly expressed, and for cells that have lower library complexity (*i.e.*, for which relatively fewer genes are detected), and results in non-random patterns in the data, whereby cells may cluster based on their complexity and genes may cluster based on their expression levels, rather than “true” co-variation. To mitigate this effect we assign weights to missing values, such that the weight of  $E_{i,j}$  is proportional to the expectation that gene  $i$  will be detected in cell  $j$  given the average expression of gene  $i$  and the total complexity (number of detected genes) of cell  $j$ .

Following PCA, we focused on the top six components as these were the only components that both explained a significant proportion of the variance and were significantly correlated with at least one gene, where significance was determined by comparison to the top 5% (of variance explained and of top gene correlations) from 100 control PCA analyses on shuffled data. PC1 had a high correlation ( $R=0.46$ ) with the number of genes detected in each cell and we did not observe a more specific biological function that may be associated with it and thus we infer this to be a technically-driven component which is reflecting the systematic variation in the data due to the large differences in the quality and complexity of data for different cells. Subsequent analysis was focused on understanding the biological function of the next components PC2-6,

which were associated with the cell cycle (PC2 and 6), regional heterogeneity (PC3) and MITF expression program (PC4 and 5).

### **Cell cycle analysis**

Our previous analysis of single-cell RNA-seq in human (293T) and mouse (3T3) cell lines (16), and in mouse hematopoietic stem cells (63), revealed in each case two prominent cell cycle expression programs that overlap considerably with genes that are known to function in replication and mitosis, respectively, and that have also been found to be expressed at G1/S phases and G2/M phases, respectively, in bulk samples of synchronized HeLa cells. We thus defined a core set of 43 G1/S and 55 G2/M genes that included those genes that were detected in the corresponding expression clusters in all four datasets from the three studies described above (Table S5). Averaging the relative expression of these gene-sets revealed cells that express primarily one of those programs, or both, while the majority of the cells do not express either of those programs (Fig. S4). We classified cells by the maximal expression of those two programs into non-cycling ( $E < 1$  or  $FDR > 0.05$ ) and cycling ( $E > 1$  and  $FDR < 0.05$ ) which were further divided into those with a low cell cycle signal ( $1 < E < 2$ ), which are likely cycling but may include some false positives or arrested cells, and those with a high signal for the cell cycle ( $E > 2$ ) which we consider as confidently cycling cells. We noticed that of the 7 tumors for which we have  $> 50$  malignant cells, 6 have either very low ( $< 3\%$ ) or very high ( $> 20\%$ ) percentage of cycling malignant cells.

### **Region-specific expression program of melanoma 79**

Genes with an average fold change  $> 3$  and  $FDR < 0.05$  (based both on a permutation test and a  $t$ -test with correction for multiple testing) in a comparison between either malignant (Fig. 2D) or CD8+ T (Fig. S6) cells from Region 1 and the corresponding cells from the other parts were

defined as preferentially expressed in region1. Malignant or CD8+ T cells from Mel79 were then sorted by their average expression of these genes.

### **MITF and AXL expression programs and cell scores**

The top 100 MITF-correlated genes across the entire set of malignant cells were defined as the MITF program, and their average relative expression as the MITF-program cell score. The average expression of the top 100 genes that negatively correlate with the MITF program scores were defined as the AXL program and used to define AXL program cell score. To decrease the effect that the quality and complexity of each cell's data might have on its MITF/AXL scores we defined control gene-sets and their average relative expression as control scores, for both the MITF and AXL programs. These control cell scores were subtracted from the respective MITF/AXL cell scores. The control gene-sets were defined by first binning all analyzed genes into 25 bins of aggregate expression levels and then, for each gene in the MITF/AXL gene-set, randomly selecting 100 genes from the same expression bin as that gene. In this way, a control gene-sets have a comparable distribution of expression levels to that of the MITF/AXL gene-set and the control gene set is 100-fold larger, such that its average expression is analogous to averaging over 100 randomly-selected gene-sets of the same size as the MITF/AXL gene-set. To calculate significance of the changes in AXL and MITF programs upon relapse, we defined the expression log<sub>2</sub>-ratio between matched pre- and post- samples for all AXL and MITF program genes (Fig. 3D). Since AXL and MITF programs are inversely related, we flipped the signs of the log-ratios for MITF program genes and used a t-test to examine if the average of the combined set of AXL program and (sign-flipped) MITF program genes is significantly higher than zero, which was the case for four out of six matched sample pairs (Fig. 3D, black arrows).

### **Cell type-specific signatures and deconvolution of bulk expression profiles**

For each of the five main cell types identified in Fig. 1 (T cells, B cells, macrophages, endothelial cells and CAFs), we defined cell type specific genes as those: **(1)** with average relative expression above 3 (i.e. approximately 8-fold higher than other cells); **(2)** expressed by >50% of the cells in that cell type; and, **(3)**  $P<0.001$  when comparing cells classified into that cell type to those in each other cell type.  $P$ -values were determined for each pairwise comparison of cell types by comparing the observed fold-change to that seen between 10,000 pairs of control sets. The control sets were generated such that each pair is mutually exclusive, has the same number of cells as classified to the two cell types, and each set is composed of equal number of cells from the two cell types. NK cells were not included in this analysis due to their small number and limited differences from T cells, and thus the T cell signature may also identify NK cells. Next, we downloaded the melanoma TCGA RNA-seqV2 expression dataset (23) and log2-transformed the RSEM-based gene quantifications and estimated the relative frequency of each cell type by the average log-transformed expression of the cell type specific genes defined above.

To identify genes that may mediate interactions between cell types we examined the correlation between the expression of genes that are expressed primarily by one cell type, based on single cell profiles, and the relative frequency of another cell type, based on bulk TCGA profiles. We focused on comparison of T cells and CAFs and identified a set of genes that although they have much higher expression in CAFs than in T cells (fold-change>4 across single cells), their expression in bulk tumors is highly correlated ( $R>0.5$ ) with the estimated relative abundance of T cells (Table S15). A similar analysis was performed for all other pairs of cell-types (Fig. S15).

### T cell classification

T cells were identified based on high expression of CD2 and CD3 (average of CD2, CD3D, CD3E and CD3G, E>4), and were further separated into CD4+, Tregs and CD8+ T cells based on the expression of CD4, CD25 and FOXP3, and CD8 (average of CD8A and CD8B),

respectively. We estimated naïve, cytotoxicity and exhaustion scores based on the average expression of the marker genes shown in Fig. 5B.

### T cell exhaustion analysis

Cytotoxicity and exhaustion scores were defined as the average relative expression of cytotoxic and exhaustion gene sets, respectively, minus the average relative expression of a naïve gene-set. Cytotoxic and naïve gene-sets correspond to the genes shown in Fig. 5B, while exhaustion was estimated with each of three alternative gene-sets: (1) the program identified in Mel75 (Fig. S21), and previously published gene-sets that represent (2) T cell exhaustion in melanoma (48) and (3) chronic viral infection (46). Importantly, even though the three gene-sets have limited overlap they give rise to similar exhaustion scores, and consequently exhaustion gene scores, as shown in Fig. 5E-F and Table S13, demonstrating the robustness of our analysis to the exact choice of initial exhaustion gene-sets. To estimate relative exhaustion of cells while controlling for the association between the expression of exhaustion and cytotoxicity markers, we first estimated the relationship between cytotoxic and exhaustion scores using a local weighted (LOWESS) regression with a window size of 75% of the cells in each tumor (black line in Fig. 5D and Fig. S23). Due to tumor-specific patterns, this analysis was restricted to the five tumors with more than 50 CD8 T cells. We then identified subsets of high exhaustion cytotoxic cells (exhaustion score - regression >0.5) and low exhaustion cells (exhaustion score – regression <-0.5), and further restricted those to cells with cytotoxic scores > -3. These thresholds were chosen to maximize the number of genes with significantly higher expression in the high-exhaustion than in the low exhaustion subsets ( $P<0.001$  by permutation test, as described above, and fold-change $>2$  in at least one tumor) (provided in Table S14). Of these, genes with  $P<0.05$  in at least three tumors were defined as consistently associated with exhaustion and are shown in Fig. 5E. Genes with  $P<0.05$  only in one or two tumors were defined as variably associated with

exhaustion and are shown in Fig. 5F. To further evaluate the significance of differential association with exhaustion across the five tumors we compared the observed fold-changes between high and low exhaustion cells in each individual tumor to that seen in 10,000 control sets of high and low exhaustion cells that contain a mix of the different tumors with equal proportions (Table S14).

### **Identification of T cell clones**

In order to detect expanded T cell clones we first mapped the transcriptome reads from each T cell to a database of TCR sequence alleles (taken from <http://www.imgt.org/>). Due to incomplete sequence coverage and sequencing errors, we did not attempt to define the exact TCR sequence of each cell but instead inferred the usage of TCR alleles, including the V and J segments of the beta and the alpha chains. We counted the number of reads, in each cell, which were mapped by Bowtie to each of these alleles with at most one mismatch. For each segment, a cell was defined as having a certain allele if at least two reads were mapped to that allele and no other allele was supported by half as many reads or more. Cells that did not have sufficient mapped reads to a certain segment, according to this criterion, were defined as unresolved. We restricted further analysis only to the cells with at least three resolved TCR segments out of the four that were examined (V and J of alpha and beta chains). We then examined all possible combinations of segments and counted, for each combination and in each tumor, the number of cells that are consistent with it and thereby define a TCR-usage cluster. Consistency was defined as having at least three identical segments and zero inconsistent segments, in order to enable cells with one unresolved segment to be classified. Cells that were consistent with multiple distinct combinations were assigned to the one with highest frequency. To evaluate the significance of clusters, we performed 1,000 simulations and compared the distribution of observed cluster sizes to the combined distribution from the simulations, focusing on Mel75. In each simulation, we

shuffled the assignment of alleles for each segment across the Mel75 cells in which that segment was resolved, thereby preserving the structure of the data while randomizing TCR-usage clustering. We separated clusters to three size ranges: 1-4 cell clusters, which were not enriched in the observed TCR usage, 5-6 cell clusters, which were enriched in the observed TCR usage but with borderline significance (FDR=0.12, defined as the fraction of cells in those clusters in the control analysis divided by the fraction of cells in the observed TCR usage), and >6 cell clusters which were highly significant (FDR=0.005). We note that most Mel75 cells assigned to this last group were part of clusters with more than 10 cells, which were never observed in the simulations and are highly unlikely to occur by chance. Apart from Mel75, we found a single TCR cluster of 11 cells in Mel74 (15% of cells included in TCR analysis), and no significant clusters in all other tumors.

### **Immunohistochemical staining**

All melanoma specimens were formalin fixed, paraffin-embedded, sectioned, and stained with hematoxylin and eosin (H&E) for histopathological evaluation at the Brigham and Women's Pathology core facility, unless otherwise specified. Immunohistochemical (IHC) studies employed 5 mm sections of formalin-fixed, paraffin-embedded tissue. All were stained on the Leica Bond III automated platform using the Leica Refine detection kit. Sections were deparaffinized and HIER was performed on the unit using EDTA for 20 minutes at 90°C. All sections were stained per routine protocols of the Brigham and Women's Pathology core facility. Additional sections were incubated for 30 min with primary antibody Ki-67 (1:250, Vector, VP-RM04) and JunB rabbit mAb (C37F9, Cell Signaling Technologies, Beverly, MA) and were then completed with the Leica Refine detection kit. The Refine detection kit encompasses the secondary antibody, the DAB chromagen (DAKO, Glostrup, Denmark) and the Hematoxilyn

counterstain. Cell counting using an ocular grid micrometer over at least five high-power fields was performed.

### **Tissue immunofluorescence staining**

Dual-labeling immunofluorescence was performed to complement immunohistochemistry as a means of two-channel identification of epitopes co-expressed in similar or overlapping sub-cellular locations. Briefly, 5-mm-thick paraffin sections were incubated with primary antibodies, AXL rabbit mAb antibody (C89E7, Abcam, Cambridge, UK) plus MITF mouse mAb (clone D5, ab3201, Abcam) and JARID1B rabbit mAb (ab56759, Abcam) plus Ki67 (ab8191, Abcam) that recognize the target epitopes at 4°C overnight and then incubated with Alexa Fluor 594-conjugated anti-mouse IgG and Alexa Fluor 488-conjugated anti-rabbit IgG (Invitrogen, Carlsbad, CA) at room temperature for 1 h. The sections were cover slipped with ProLong Gold anti-fade with DAPI (Invitrogen). Sections were analyzed with a BX51/BX52 microscope (Olympus America, Melville, NY), and images were captured using the CytoVision 3.6 software (Applied Imaging, San Jose, CA). The following primary antibodies were used for staining per manufactures recommendations: mouse anti-MITF (DAKO), rabbit ant-AXL (Cell Signaling), goat anti-TIM3 (R&D Systems, Minneapolis, MN), rabbit ant-PD1 (Sigma Aldrich, St. Louis, MO), and goat anti-PD1 (R&D Systems).

### **Cell culture experiments and AXL flow-cytometry**

Cell lines listed in Table S11 from the Cancer Cell Encyclopedia Lines (35) were used for flow-cytometry analysis of the proportion of AXL-positive cells. Based on IC<sub>50</sub> values for vemurafenib, we selected seven cell lines that were predicted to be sensitive to MAP-kinase pathway inhibition, including WM88, IGR37, MELHO, UACC62, COLO679, SKMEL28 and A375 and three cell lines predicted to be resistant, including IGR39, 294T and A2058. These ten

cell lines were used for drug sensitivity testing and pre-treatment and post-treatment analysis of the AXL-positive fraction. For WM88, IGR37, MELHO, UACC62, COLO679, SKMEL28 and A375, cells were plated at a density to be at 30-50% confluent after 16 hours post seeding. A total of four drug arms were plated for each cell line using two T75 (Corning, Corning, NY) and two T175 (Corning) culture flasks. Approximately 16-24 hours after seeding, cells were treated with DMSO or dabrafenib (D) (Selleck, Houston, TX) and trametinib (T) (Selleck) at the following drug doses of D/T: 0.01uM/0.001uM, 0.1uM/0.01uM and 1uM/0.1uM (T175 reserved for higher drug concentrations). Cells were maintained in drug for a total of 5 days, at which point, cells were harvested for flow sorting. For IGR39, 294T and A2058, cells were plated at a density to be at 20-30% confluent 16 hours post seeding. Cells were treated with the DMSO or D/T at using the same doses as above and maintained in drug for a total of 10 days, at which point, cells were harvested for flow sorting. For AXL-flow sorting, cells were first washed with warm PBS, followed by an addition of 10mM EDTA and incubated for 2 minutes at room temperature. Excess EDTA was then aspirated and cells incubated at 37°C until cells detached from flask. Cells were resuspended in cold PBS 2% FBS and kept on ice. Cells were counted and 500,000 cells were transferred to 15ml conical tubes (Falcon), spun down and resuspended in 100 $\mu$ l of cold PBS 2% FBS alone (negative control) or antibodies using manufacturers recommendations, including 1 $\mu$ g of AXL antibody (AF154, R&D Systems) or 1 $\mu$ g of normal goat IgG control (Isotype control, AB-108-C, R&D Systems). Cells were incubated on ice for 1 hour, then washed twice with cold PBS 2% FBS. Cells were pelleted and resuspended in 100 $\mu$ l PBS 2% FBS with 5 $\mu$ l of Goat IgG (H+L) APC-conjugated Antibody (F0108, R&D Systems) and incubated for 30 minutes at room temperature. Cells were then washed twice with cold PBS 2% FBS, pelleted and resuspended in 500 $\mu$ l of PBS 2% FBS and transferred to 5mL flow-cytometry tubes (Falcon). 1 $\mu$ l of SYTOX Blue Dead Stain (Thermo Fisher) was added to each sample and samples analyzed by flow-cytometry. Data was analyzed using FACSDiva Version

6.2 using viable cells only (as determined by SYTOX Blue staining) and gates for AXL-positivity were set using the Isotype control set to <1%.

### **Single-cell immunofluorescence staining and analysis**

For single-cell immunofluorescence (single-cell IF) studies, we included the following cell lines from CCLE: WM88, MELHO, SKMEL28, COLO679, IGR39, A2058 and 294T. Cells were cultured and detached as described above, and seeded at a density of 10,000 cells per well into Costar 96-well black clear-bottom tissue culture plates (3603, Corning). Cells were treated using Hewlett-Packard (HP) D300 Digital Dispenser with vemurafenib (Selleck) alone or in combination with trametinib (Selleck) at indicated doses for 5 and 10 days. In the case of 10-day treatment, growth medium was changed after 5 days followed by immediate drug re-treatment. Cells were then fixed in 4% paraformaldehyde for 20 minutes at room temperature and washed with PBS with 0.1% Tween 20 (Sigma-Aldrich) (PBS-T), permeabilized in methanol for 10 min at room temperature, rewashed with PBS-T, and blocked in Odyssey Blocking Buffer for 1 hour at room temperature. Cells were incubated overnight at 4°C with primary antibodies in Odyssey Blocking Buffer. The following primary antibodies with specified animal sources and catalogue numbers were used in specified dilution ratios: p-ERK<sup>T202/Y204</sup> rabbit mAb (clone D13.14.4E, 4370, Cell Signaling Technology), 1:800, AXL goat polyclonal antibody (AF154, R&D Systems), 1:800, MITF mouse mAb (clone D5, ab3201, Abcam), 1:400. Cells were then stained with rabbit, mouse and goat secondary antibodies from Molecular Probes (Invitrogen) labeled with Alexa Fluor 647 (A31573), Alexa Fluor 488 (A21202), and Alexa Fluor 568 (A11057). Cells were washed once in PBS-T, once in PBS and were then incubated in 250 ng/ml Hoechst 33342 and 1:800 Whole Cell Stain (blue; Thermo Scientific) solution for 20 min. Cells were washed twice with PBS and imaged with a 10× objective on a PerkinElmer Operetta High Content Imaging System. 9-11 sites were imaged in each well. Image segmentation, analysis and

signal intensity quantitation were performed using Acapella software (Perkin Elmer). Population-average and single-cell data were analyzed using MATLAB 2014b software. Single-cell density scatter plots were generated using signal intensities for individual cells.

### **CAF-melanoma co-cultures from melanoma 80**

Solid tumor sample was removed from the transport media (Day 1: date of procurement) and minced mechanically in DMEM culture media (ThermoFisher Scientific), 10% FCS (Gemini Bioproducts), 1% pen/strep (Life Technologies) on 10 cm culture plates (Corning Inc.) and left overnight in standard culture condition (37C, humidified atmosphere, 5% CO<sub>2</sub>). The liquid media in which the procured tissue was originally placed was spun down (1500 rpm) to isolate the detached cells in solution and the pelleted cells were resuspended in fresh culture media and propagated in culture flasks (Corning Inc.) (fraction 1). The minced tumor samples were removed from the 10 cm culture dishes on Day 2 and mechanically forced through 100 uM nylon mesh filters (Fisher Scientific) using syringe plungers and washed through with fresh culture media. The cells and tissue clumps were spun down in 50 ml conical tubes (BD Falcon), resuspended in fresh culture media, and propagated in culture flasks (fraction 2). The 10 cm culture dishes in which the samples had been minced and placed overnight were washed replaced with fresh culture media so that the attached cells could be propagated (fraction 3). Cells were propagated by changing culture media every 3-4 days and passaging cells in 1:3 to 1:6 ratio using 0.05% trypsin (Thermo Scientific) when the plates became 50-80% confluent.

### **Tissue microarray staining, image acquisition and analysis**

We purchased two individual melanoma tissue microarrays (TMAs), including ME208 (US Biomax, Rockville, MD) and CC38-01-003 (Cybrdi, Rockville, MD). These contained a total of 308 core biopsies, including a total of 180 primary melanomas, 90 metastatic lesions, 18

melanomas with adjacent healthy skin and 20 healthy skin controls. Each TMA was double-stained with conjugated complement 3-FITC antibody (F0201, DAKO) and CD8-TRITC (ab17147, Abcam) per manufacturers recommendations. Image acquisition was performed on the RareCyte CyteFinder high-throughput imaging platform (64). For each TMA-slide, the 3-channel (DAPI/FITC/TRITC) 10 $\times$  images were captured and stored as Bio-format stacks. The image stacks were background-subtracted with rolling ball method and stitched into single image montage of each channel using ImageJ. For the quantification of CD8/C3 positive area and signal intensity, the gray-scale images were converted into binary images with the Otsu thresholding method (65, 66). Each tissue spot was segmented manually and DAPI, C3 and CD8-positive areas and intensities were calculated using ImageJ (NIH, MD). In order to control for sample quality, core biopsies with a DAPI staining less than 10% of total area were excluded from the correlation analysis. The raw numerical data were then processed and Pearson's correlation coefficients were calculated between C3/CD8 area fraction and intensity using MATLAB 2014b software (MathWorks, MA)

## **Supplementary Figures and Tables**

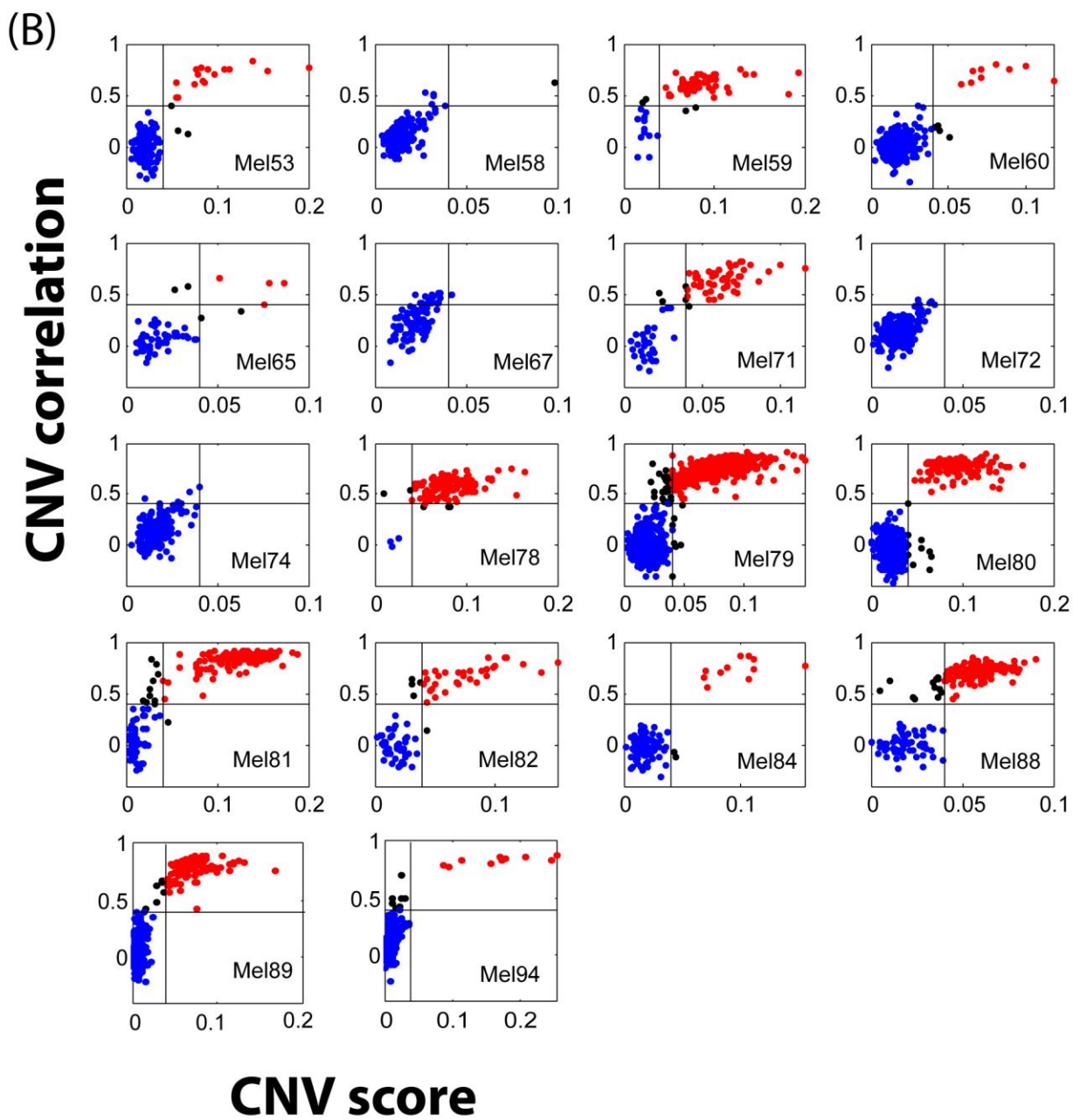
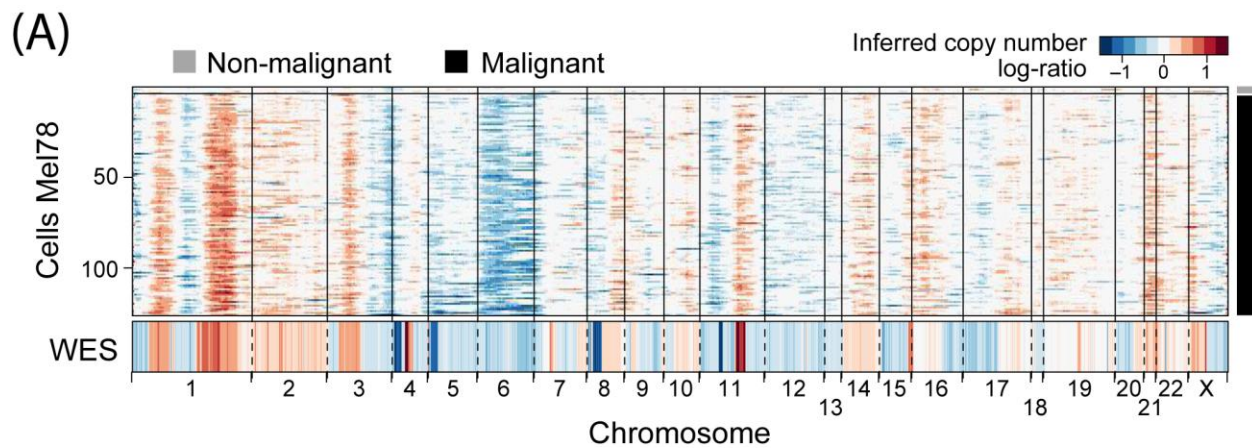
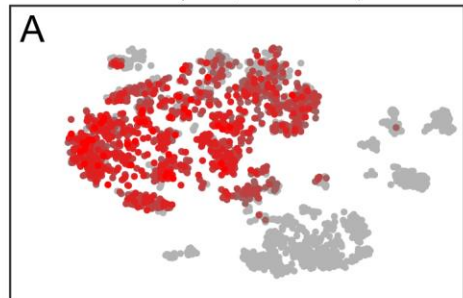


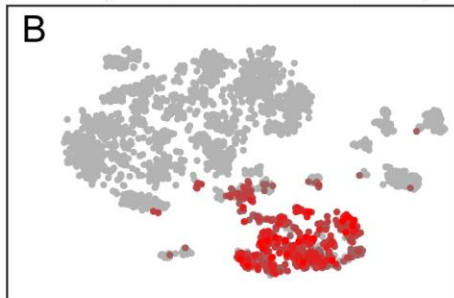
**Figure S1. Classification of cells to malignant and non-malignant based on inferred CNV patterns.**

(A) Same as shown in Fig. 1B for another melanoma tumor (Mel78). (B) Each plot compares two CNV parameters for all cells in a given tumor: (1) CNV score (X-axis) reflects the overall CNV signal, defined as the mean square of the CNV estimates across all genomic locations; (2) CNV correlation (Y-axis) is the Pearson correlation coefficient between each cell's CNV pattern and the average CNV pattern of the top 5% of cells from the same tumor with respect to CNV signal (i.e., the most confidently-assigned malignant cells). These two values were used to classify cells as malignant (red; CNV score  $> 0.04$ ; correlation score  $> 0.4$ ; grey lines mark thresholds on plot), non-malignant (blue; CNV score  $< 0.04$ ; correlation score  $< 0.4$ ), or unresolved intermediates (black, all remaining cells). In four tumors (Mel58, 67, 72 and 74), we sequenced primarily the immune infiltrates (CD45+ cells) and there were only zero or one malignant cells by this definition; in those cases, CNV correlation is not indicative of malignant cells (since the top 5% cells by CNV signal are primarily non-malignant) and therefore all cells except for one in Mel58 were defined as non-malignant. Note that while these thresholds are somewhat arbitrary, this classification was highly consistent with the clustering patterns of these cells (as shown in Fig. 1C) into clusters of malignant and non-malignant cells.

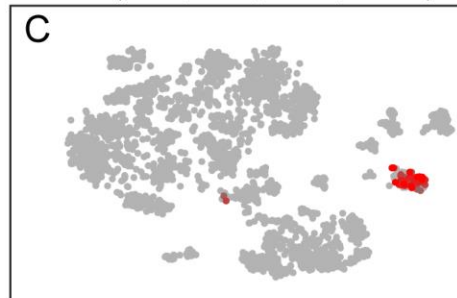
T-cell (CD2,CD3D/E/G)



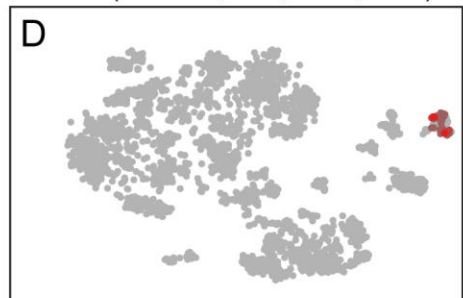
B-cell (CD19,CD20,CD79A/B,BLNK)



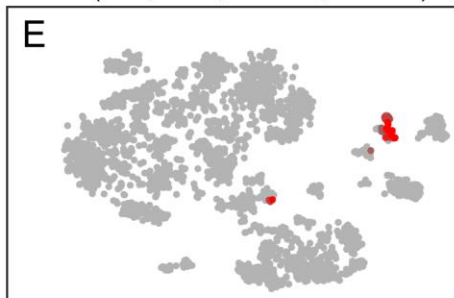
Macro.(CD14,CD68,CD163,CSF1R)



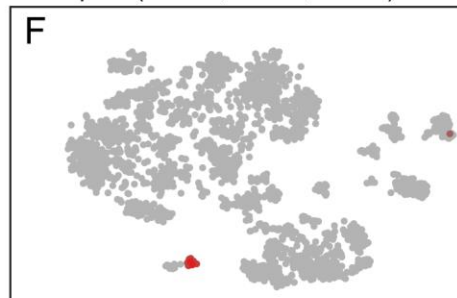
Endo. (PECAM1,VWF,CDH5,SELE)



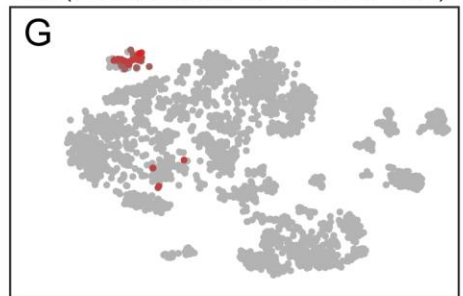
CAF (FAP,CD90,COL1A1,COL3A1)



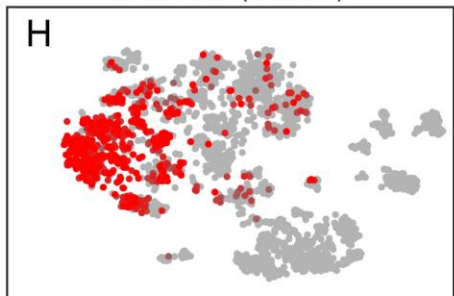
pDC (CD123,CD303,CD304)



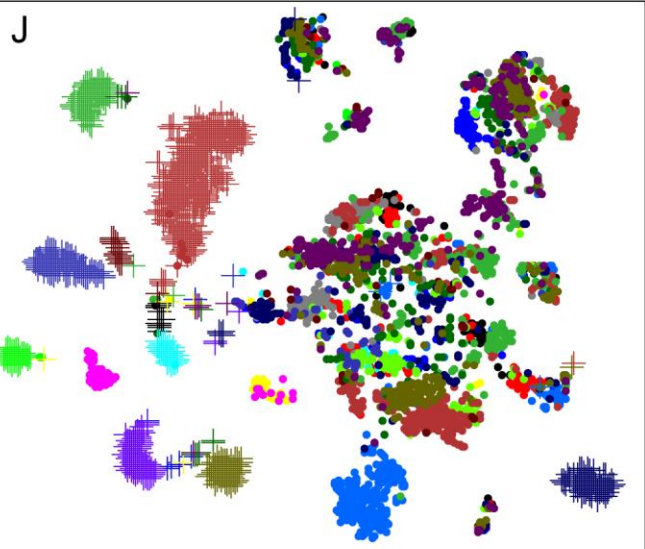
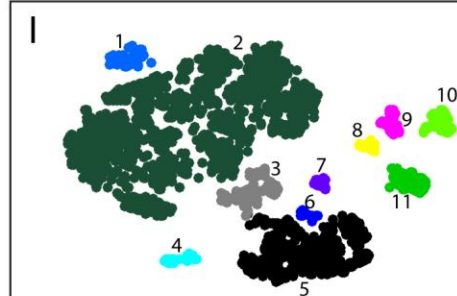
NK (CD16,CD56,KLRB1/C1/D1/F1/K1)



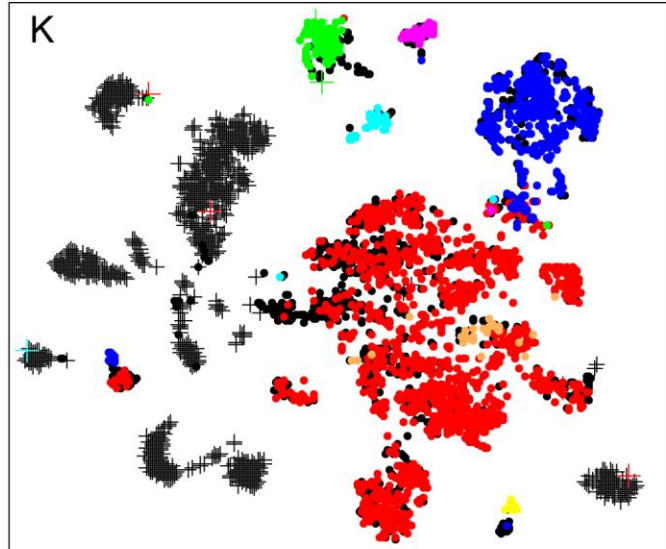
CD8 T-cell (CD8A/B)



DBscan clusters



- Mel53
- Mel58
- Mel59
- Mel60
- Mel65
- Mel67
- Mel71
- Mel72
- Mel74
- Mel75
- Mel78
- Mel79
- Mel80
- Mel81
- Mel84
- Mel88
- Mel89
- Mel94

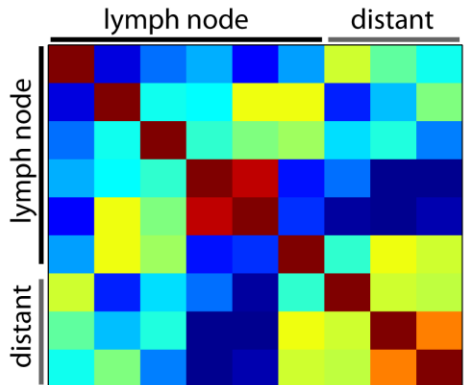


#### Expression of cell type markers:

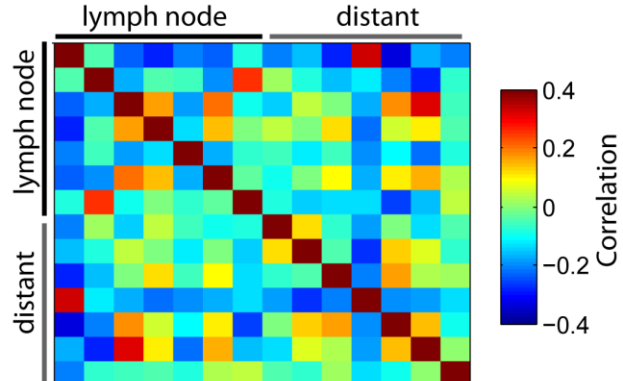
- |          |          |       |      |
|----------|----------|-------|------|
| • T-cell | • Macro. | • CAF | • NK |
| • B-cell | • Endo.  | • pDC |      |

**Figure S2. Identification of non-malignant cell types by tSNE clusters that preferentially express cell type markers.** (A–H) Each plot shows the average expression of a set of known marker genes for a particular cell type (as indicated at the top) overlaid on the tSNE plot of non-malignant cells, as shown in Fig. 1C. Gray indicates cells with no or minimal expression of the marker genes ( $E$ , average  $\log_2(\text{TPM}+1)$ , below 4), dark red indicates intermediate expression ( $4 < E < 6$ ), and light red indicates cells with high expression ( $E > 6$ ). (I) DBscan clusters derived from tSNE coordinates, with parameters  $\text{eps}=6$  and  $\text{min-points}=10$ . Eleven clusters are indicated by numbers and colors. (J–K) Combined tSNE plot of all cells profiled in this work. Colors indicate the tumor-of-origin in (J) and the expression of cell type-specific marker genes ( $E > 5$ ) in (K).

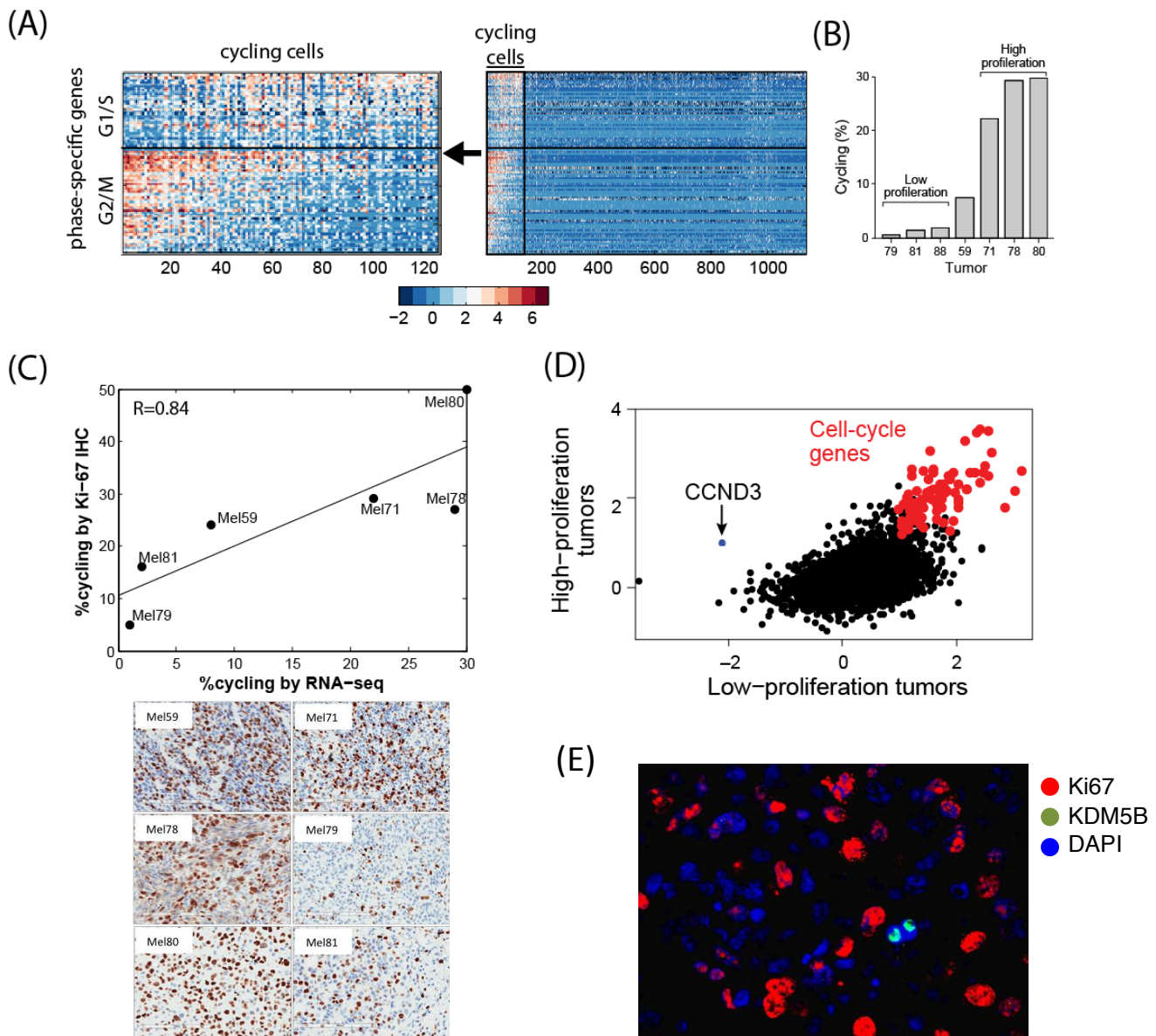
(A) Melanoma cells



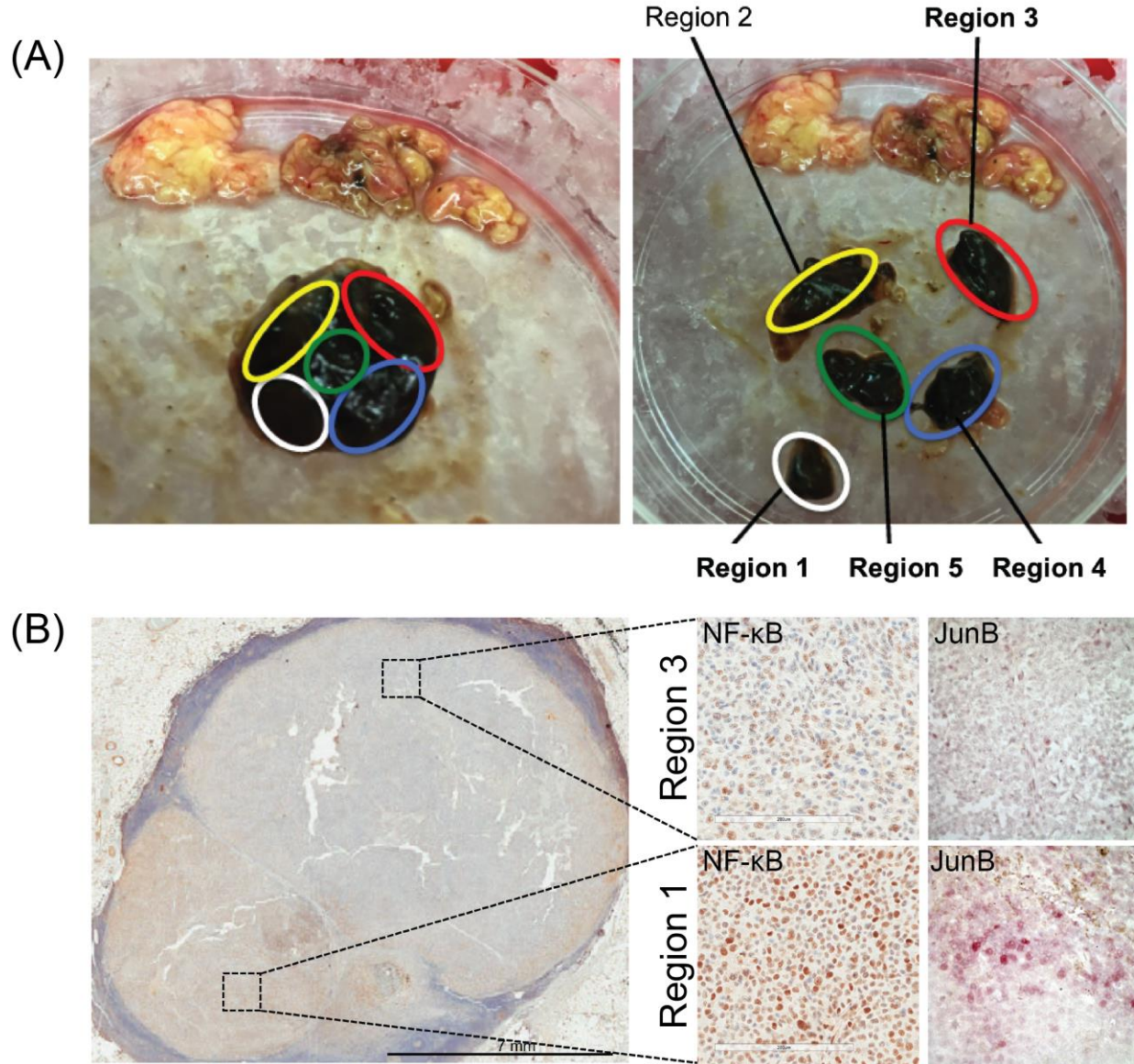
(B) T cells



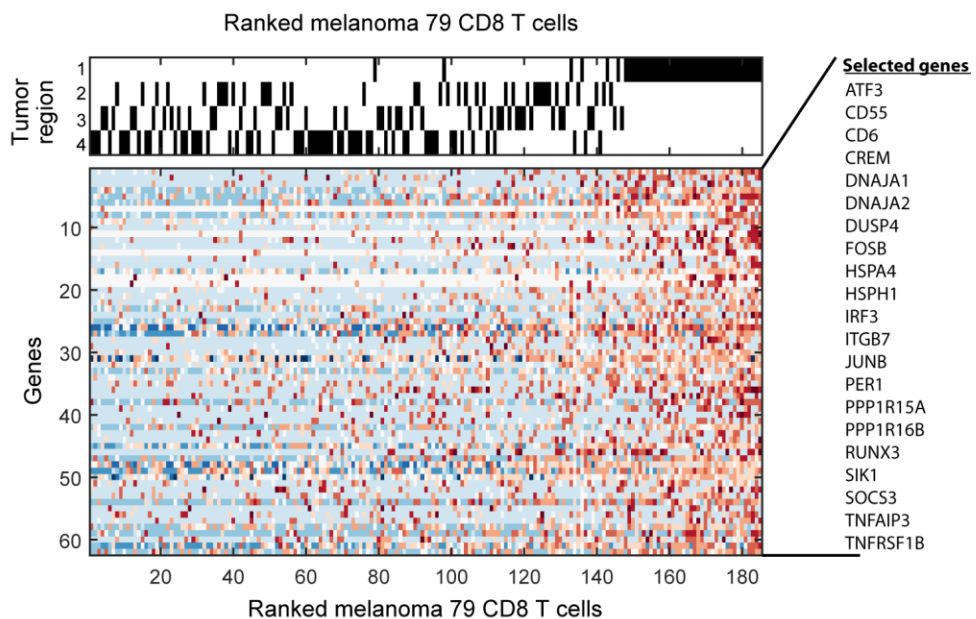
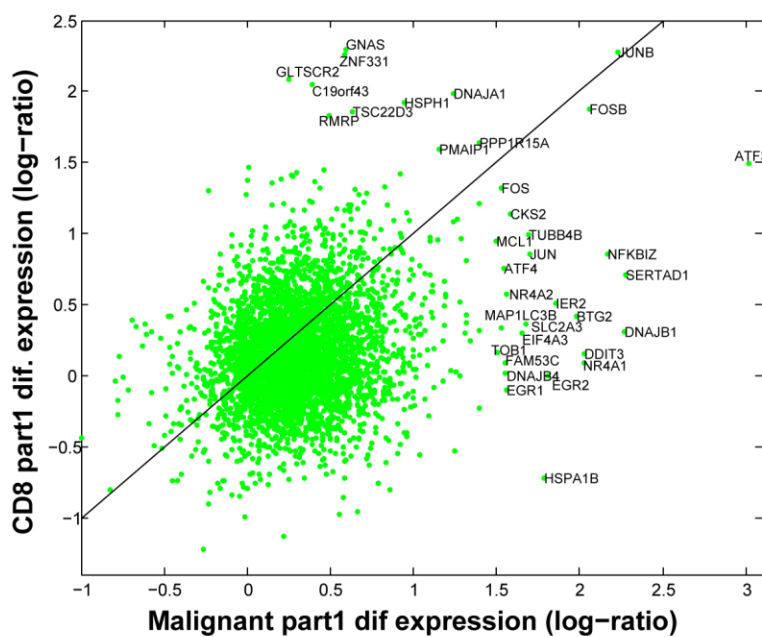
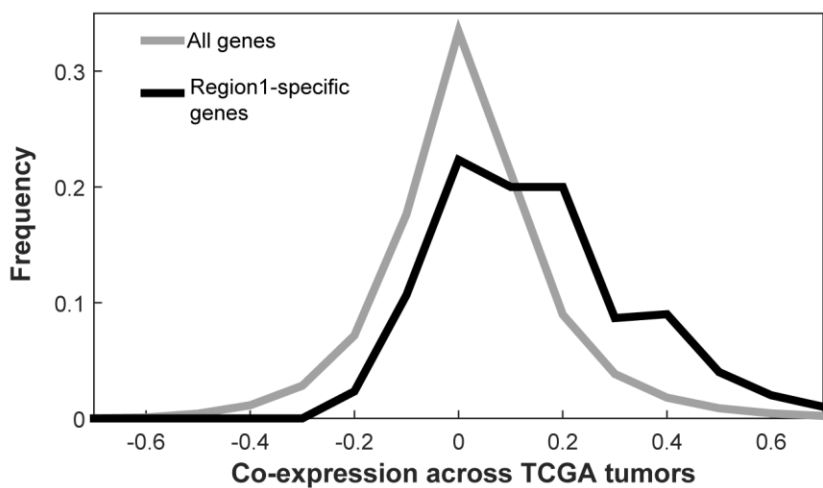
**Figure S3. Limited influence of tumor site on RNA-seq patterns.** (A–B) Heat maps show correlations of global expression profiles between tumors, which were ordered by metastatic site. Expression levels were first averaged over melanoma (A) or T cells (B) in each tumor and then centered across the different tumors before calculating Pearson correlation coefficients. Differential expression analysis conducted between the two groups of tumors found zero differentially expressed genes with FDR of 0.05 based on a shuffling test for both T cells and melanoma cells.



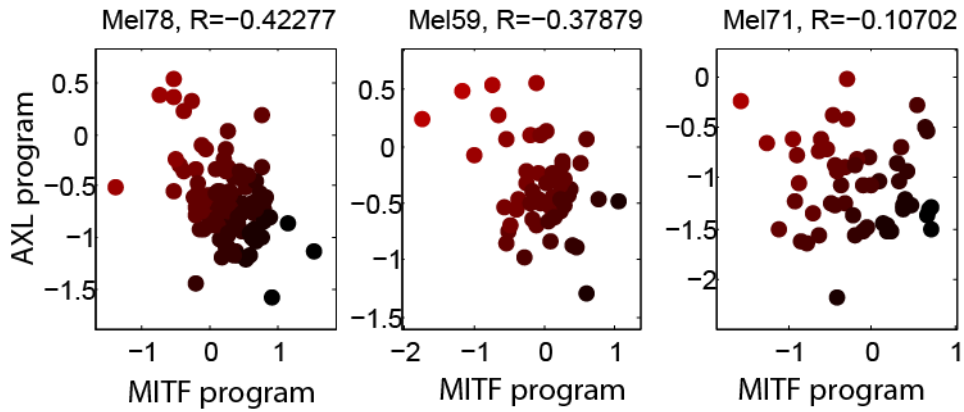
**Figure S4. Identification and characterization of cycling malignant cells.** (A) Heat map showing relative expression of G1/S (top) and G2/M (bottom) genes (rows, as defined from integration of multiple datasets; **Methods**) across cycling cells (left panel, columns, ordered by the ratio of expression of G1/S genes to G2/M genes) and across all cells (right panel, columns, cycling cells ordered as in left panel followed by non-cycling cells at random order). Cycling cells were defined as those with significantly high expression of G1/S and/or G2/M genes (FDR<0.05 by *t*-test, and fold-change > 4 compared to all malignant cells). (B) The frequency of inferred cycling cells (Y axis) in seven tumors (X axis) with > 50 malignant cells/tumors, denoting low ( $\leq 3\%$ ) or high ( $>20\%$ ) proliferation tumors. (C, upper panel) Significant correlation ( $P < 0.038$ ) between inferred proportion of cycling cells by single-cell transcriptome analysis (horizontal axis) and Ki67+ immunohistochemistry (IHC) (lower panel) of corresponding tumor slides (vertical axis). (D) Comparison of cycling cell expression programs between low- and high-proliferation tumors. Scatter plots compared the expression log-ratio between cycling and non-cycling cells in high-proliferation (y-axis) and low-proliferation (x-axis) tumors. Genes significantly upregulated ( $P < 0.01$ , fold-change  $> 2$ ) in cycling cells in both types of tumor are marked in red. *CCND3* (arrow) is significantly upregulated in cycling cells in high-proliferation tumors and downregulated in cycling cells in low-proliferation tumors. (E) Dual KDM5B (JARID1B)/Ki67 immunofluorescence staining of tissue slide of Mel80 (40x magnification). Consistent with findings presented for Mel78 and Mel79 in Fig. 2C, KDM5B-expressing cells (green nuclear staining) occurred in small clusters of two or more cells and do not express Ki67 (red nuclear staining), indicating that these cells are not undergoing cell division.



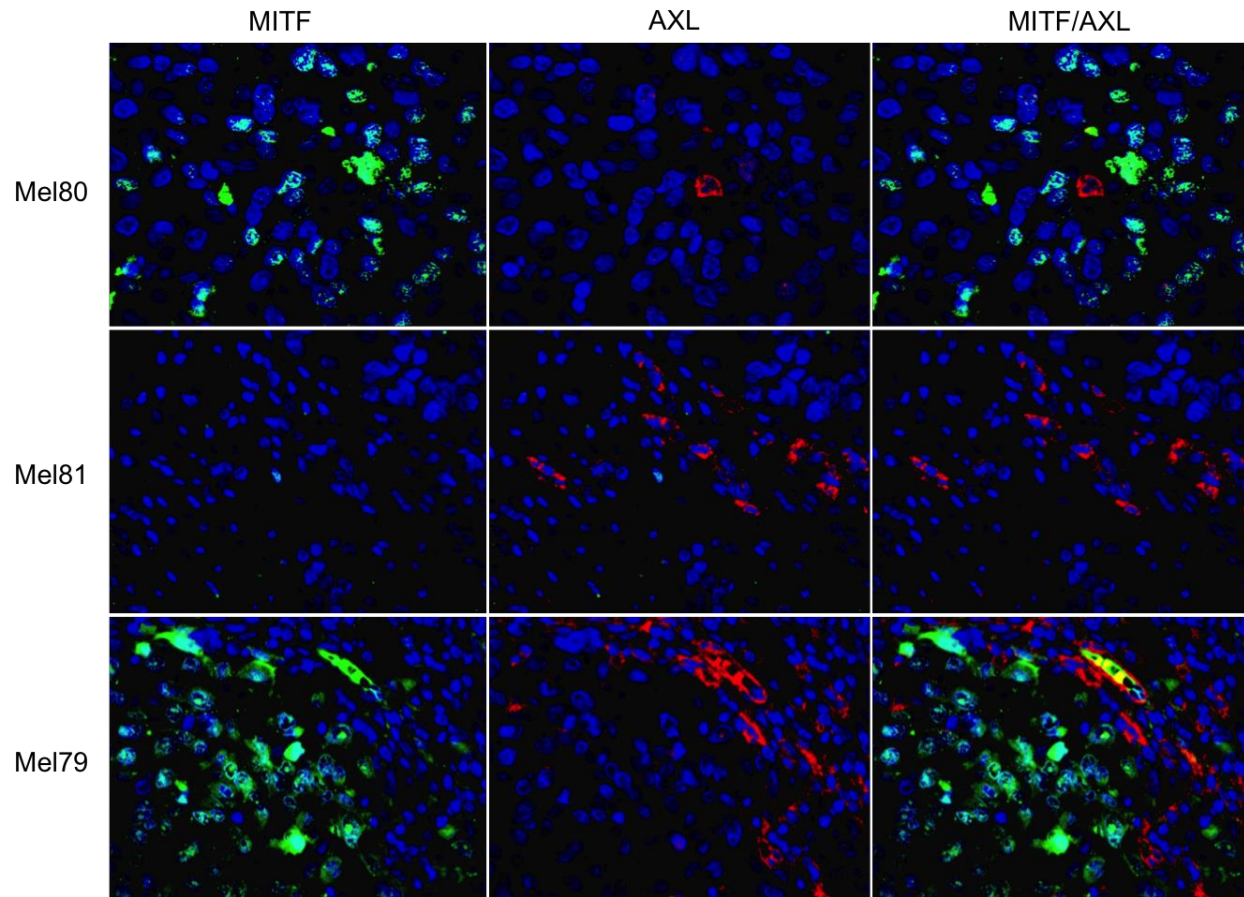
**Figure S5. Immunohistochemistry of melanoma 79 shows gross differences between tumor parts and increased NF-κB levels in Region 1.** (A) Tumor dissection into five regions. Left: melanoma tumor prior to dissection. Macroscopically distinct regions are highlighted by colored ovals. Right: The tumor was dissected into five pieces, which were further processed as individual samples. Regions 1, 3, 4 and 5 were included in the single-cell RNA-seq analysis, Cells from Region 2 were lost during library construction. (B) Corresponding histopathological cross-section of the tumor demonstrates distinct features of Region 1 compared to the other regions. Consistent with enrichment of cells in Region 1 expressing multiple markers that are highlighted in Fig. 2D, immunohistochemistry staining revealed increased staining of NF-κB and JunB in Region 1 (right lower panel, 40x magnification), compared to region Region 3 (right upper panel, 40xmagnification).

**A****B****C**

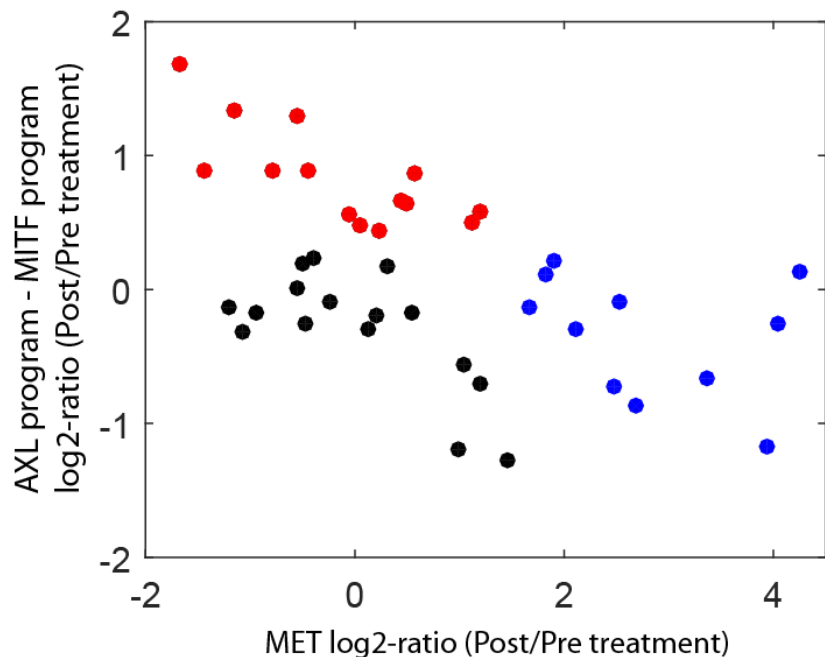
**Figure S6. Spatial heterogeneity in Mel79.** **(A-B)** As shown in Fig. 2D for malignant cells, we examined the expression differences between regions of Mel79 for other cell types. The only cell type for which we had >10 cells in each of the regions was CD8+ T cells. We thus focused on the differences among CD8+ T cells and found 62 genes that were preferentially expressed in region 1 (fold-change>2, FDR<0.05) and that partially overlapped the region 1-specific genes among the malignant cells (see Table S6). **(A)** Region 1-specific expression program of CD8+ T-cells (as shown in Fig. 2D for malignant cells). Bottom: heat map shows the relative expression of the 62 genes preferentially expressed in region 1, in all CD8+ T-cells from Mel79, ranked by their average expression of these genes. A subset of genes of interest are noted at the right. Top: assignment of cells to the four regions of Mel79. **(B)** Comparison of region 1 preferential expression between malignant cells (X-axis) and CD8+ T-cells (Y-axis). For each cell type, the scatterplot shows the log2-ratio between the average expression of all cells in region 1 and those in all other regions. **(C)** The top region1-specific genes from analysis of malignant cells (25 genes with 3-fold upregulation in region 1 compared to all other regions of Mel79) are co-expressed across melanoma TCGA bulk tumors. Shown are the distribution of Pearson correlation coefficients among the expression profiles of the top region1-specific genes (black), which is significantly higher ( $P<0.001$  by permutation test) than the distribution of correlations among all genes (gray).



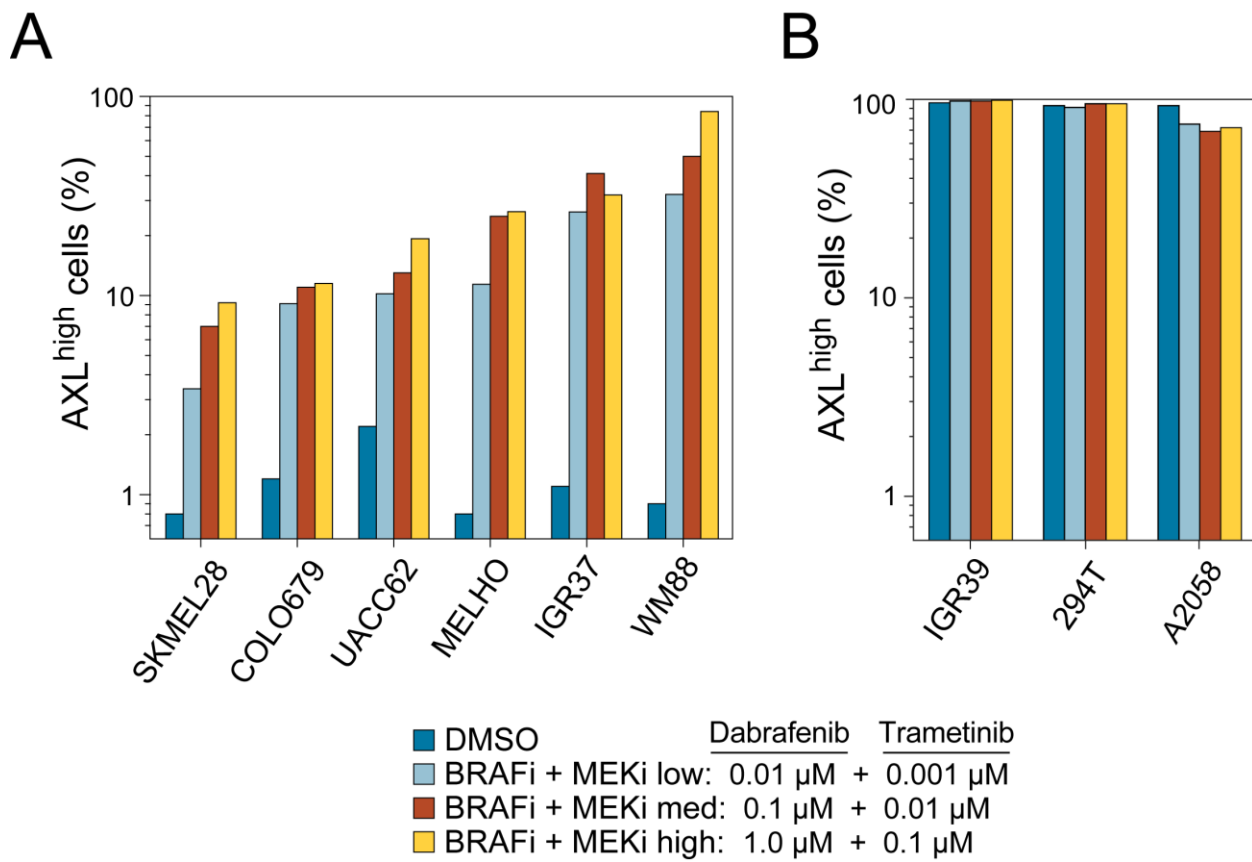
**Figure S7. Intra-tumor heterogeneity in AXL and MITF programs.** AXL-program (Y-axis) and MITF-program (X-axis) scores for malignant cells in each of the three tumors with a sufficient number of malignant cells ( $n > 50$ ) that were not included in Fig. 3B. Cells are colored from black to red by the relative AXL and MITF scores. The Pearson correlation coefficient is denoted on top.



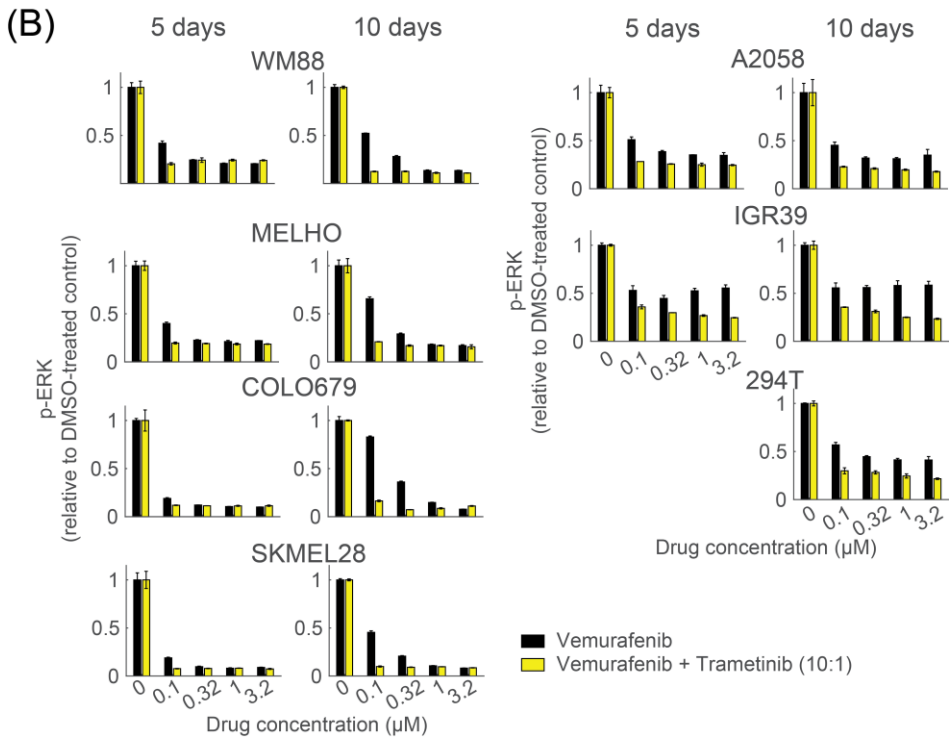
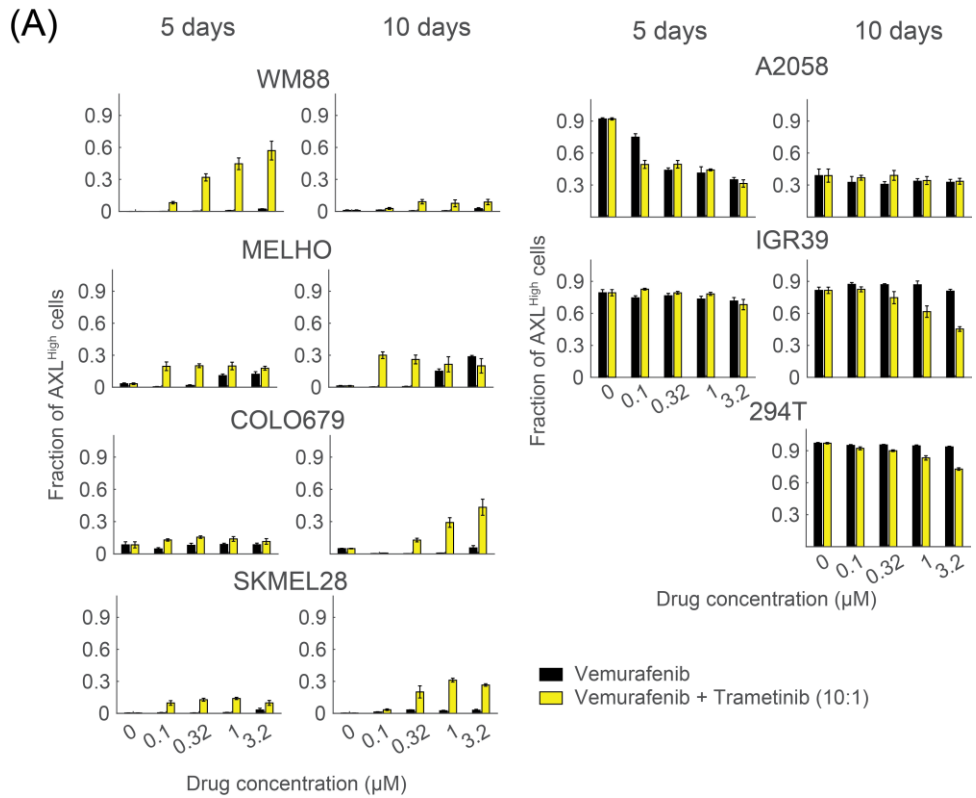
**Figure S8.** AXL/MITF immunofluorescence staining of tissue slides of Mel80, Mel81 and Mel79 (40x magnification) revealed presence of AXL-expressing and MITF-expressing cells in each sample. Consistent with single-cell RNA-seq inferred frequencies of each population, Mel80 contained rare AXL-expressing cells (red, cell membrane staining) and mostly malignant MITF-positive cells (green, nuclear staining), while malignant cells of Mel81 almost exclusively consisted of AXL-expressing cells. Mel79 had a mixed population with rare cells positive for both markers, all in agreement with the inferred single-cell transcriptome data.



**Figure S9. AXL upregulation in a second cohort of post-treatment melanoma samples and mutual exclusivity with MET upregulation.** Each point reflects a comparison between a matched pair of pre-treatment and post-relapse samples from Hugo et al. (33), where the X-axis shows expression changes in MET, and the Y-axis shows expression changes in the AXL program minus those of the MITF program. Note that some patients are represented more than once based on multiple post-relapse samples. Fourteen out of 41 samples (34%) shown in red had significant upregulation of the AXL vs. MITF program, as determined by a modified t-test as described in Methods; these correspond to at least one sample from half (9/18) of the patients included in the analysis. Eleven out of 41 samples (27%) shown in blue had at least 3-fold upregulation of MET; these correspond to at least one sample from a third (6/18) of the patients included in the analysis. Notably, the AXL and MET upregulated samples are mutually exclusive, consistent with the possibility that these are alternative resistance mechanism.



**Figure S10. Flow-cytometry of melanoma cell lines before and after treatment with RAF/MEK-inhibition.** (A) Sensitive cell lines show an increased proportion of AXL-positive cells while resistant cell lines (B) show modest or no changes following treatment with RAF/MEK-inhibitors.



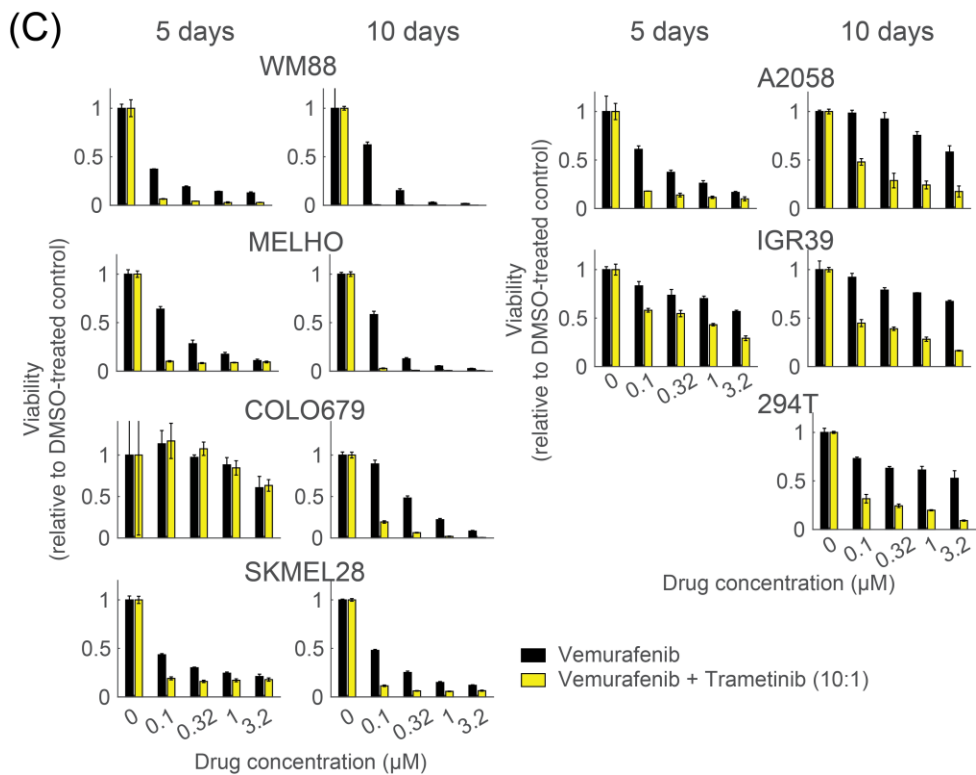
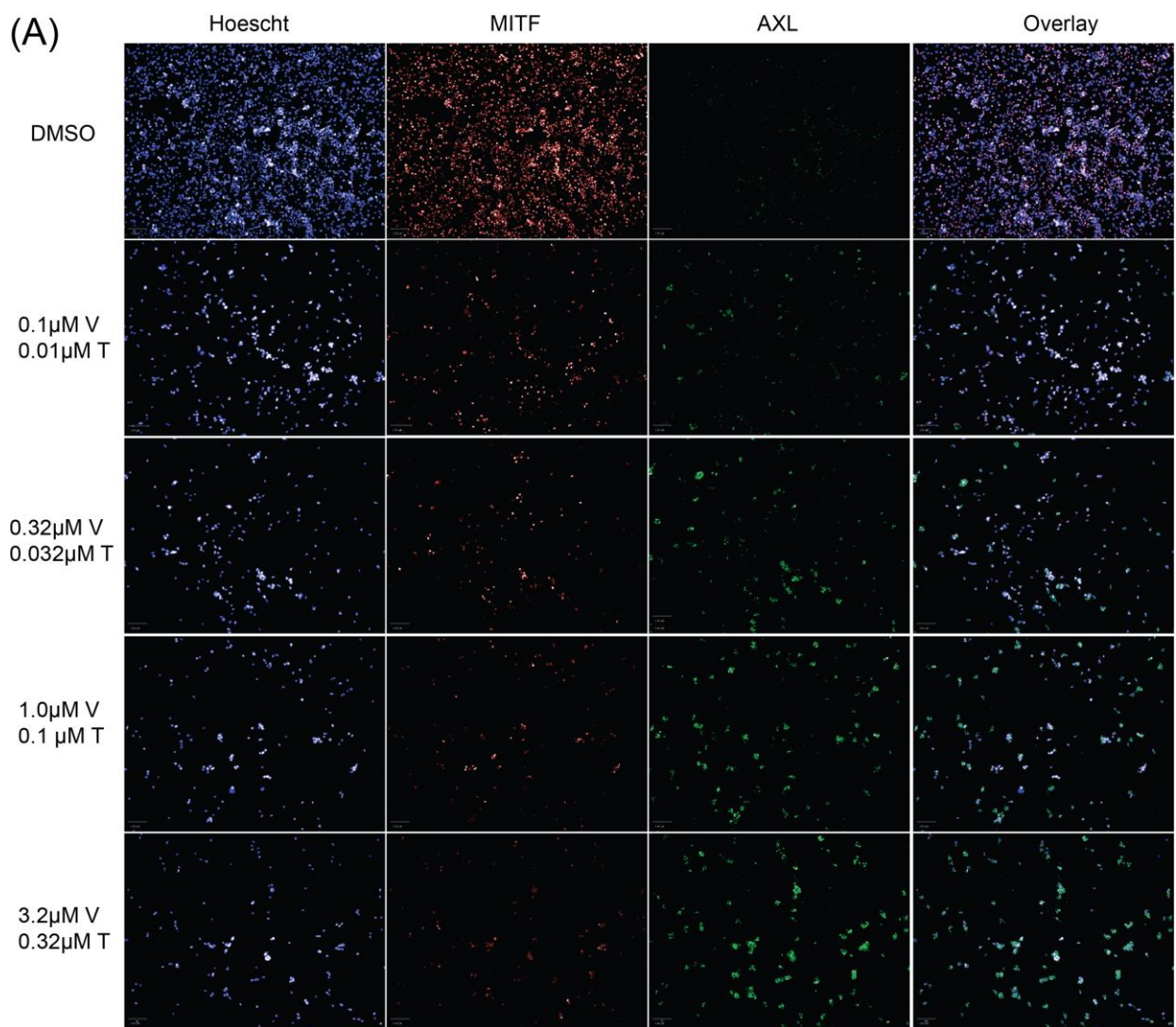


**Figure S11. Summary of multiplexed single-cell immunofluorescence in seven CCLE cell lines before and after treatment with BRAF/MEK-inhibition.** (A) Relative fraction (compared to DMSO-treatment) of AXL-high cells (y-axis) treated for 5 or 10 days with increasing doses (as indicated on x-axis) of BRAF-inhibition alone (with vemurafenib) or in combination with a MEK-inhibitor (trametinib) with a 10:1 ratio (vemurafenib:trametinib). In all cell lines with a baseline low-fraction of AXL-expressing cells (WM88, MELHO, COLO679 and SKMEL28), there was a significant dose-dependent increase in the AXL-high cell fraction with BRAF-inhibition alone (black bars), and more pronounced with combined BRAF/MEK-inhibition (yellow bars). Cell lines with a baseline high AXL-expressing cell fraction (A2058, IGR39 and 294T) showed either minimal changes in the AXL-high cell fraction, however, A2058 demonstrated a significant decreased in the AXL-positive fraction. Although an outlier in this experiment, this indicates that alternative mechanisms of resistance with low AXL expression (Hugo et al. (33); Figure S9). (B) The increase in AXL-high cell fractions in the sensitive cell lines was correlated with a significant decrease of p-ERK indicating strong MAP-kinase pathway inhibition, and (C) a decrease in cell viability. Overall, these results indicate, that the increase in the AXL-high cell fraction was at least in part due to a selection process. Both effects were more pronounced when cells were treated with combined BRAF/MEK-inhibition compared BRAF-inhibition alone.



(B)

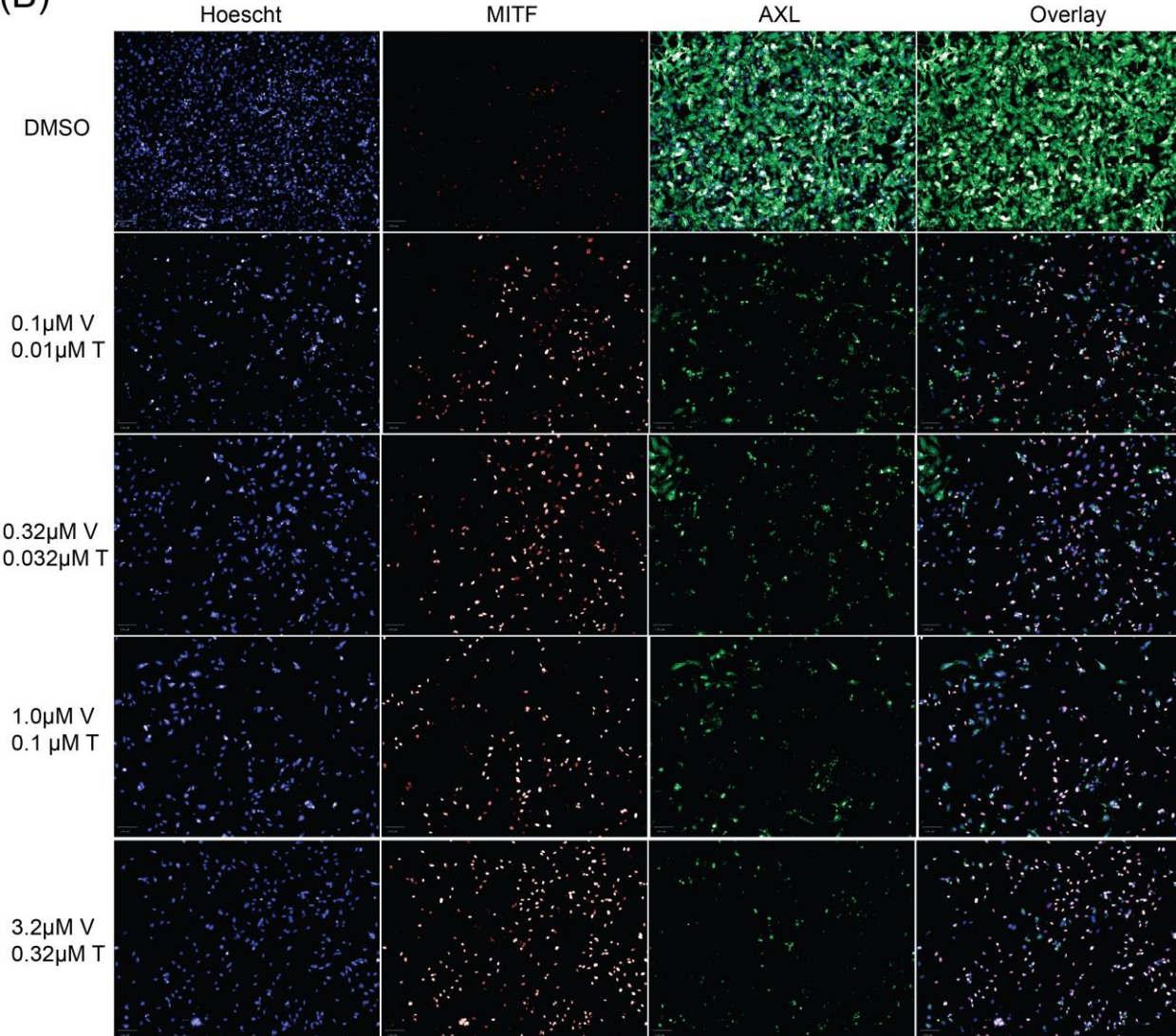


**Figure S12.** Exemplary images of multiplexed single-cell immunofluorescence quantitative analysis for **(A)** an AXL-low (WM88) and **(B)** AXL-high cell line (A2058). Treatment with a combination of vemurafenib (V) and trametinib (T) at indicated doses on the left resulted in a dose-dependent change in the AXL-high population. In WM88, increasing drug concentrations led to killing of MITF-expressing, resulting in the emergence of a pre-existing AXL-high subpopulation. This indicates that the shift towards a higher AXL-expressing population (and possibly the AXL-high signature) is at least in part due to a selection process. While cell lines with a high baseline fraction of AXL-expressing cells showed modest to no changes in the AXL-fraction (Fig. S10B), A2058 was an exception. This cell lines has a major AXL-expressing population at baseline, which decreases with treatment, while the MITF-expressing population emerges. This indicates the presence of alternative mechanisms of resistance to RAF/MEK-inhibition, consistent with a recent report by Hugo et al. (33) and our analysis shown in Fig. S9.

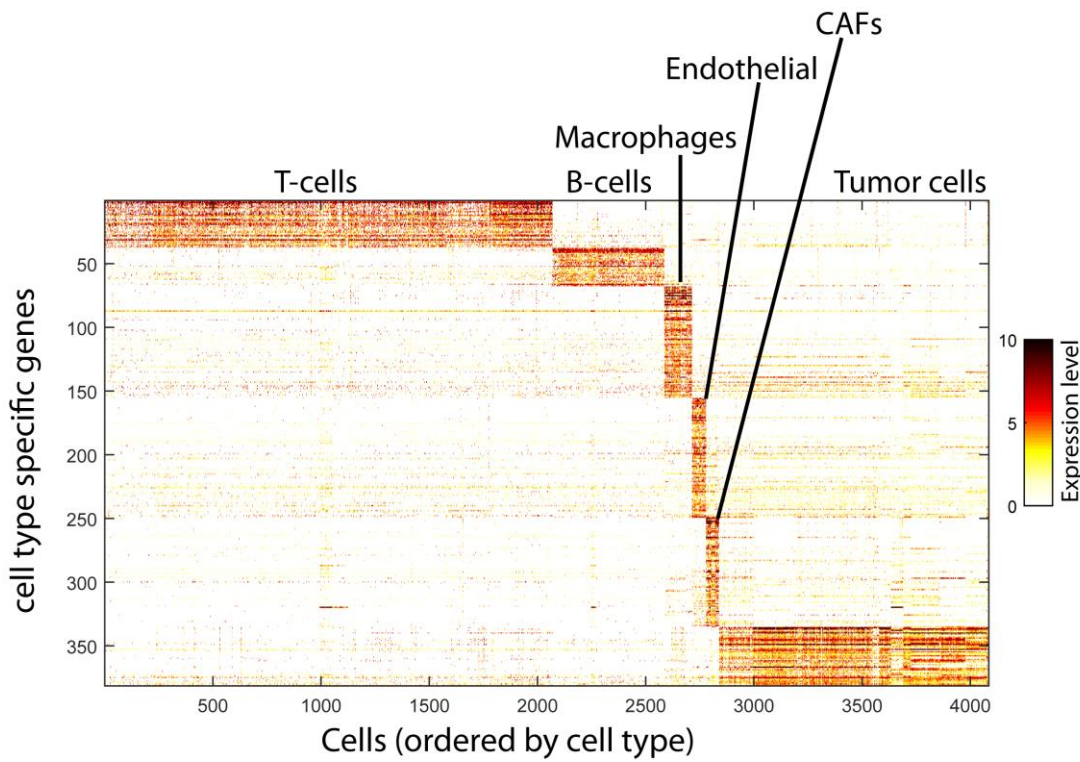


**Figure S13. Identification of cell-type specific genes in melanoma tumors.** Shown are the cell-type specific genes (rows) as chosen from single cell profiles (**Methods**), sorted by their associated cells cell type, and their expression levels ( $\log_2(\text{TPM}/10+1)$ ) across non-malignant and malignant tumor cells, also sorted by type (columns).

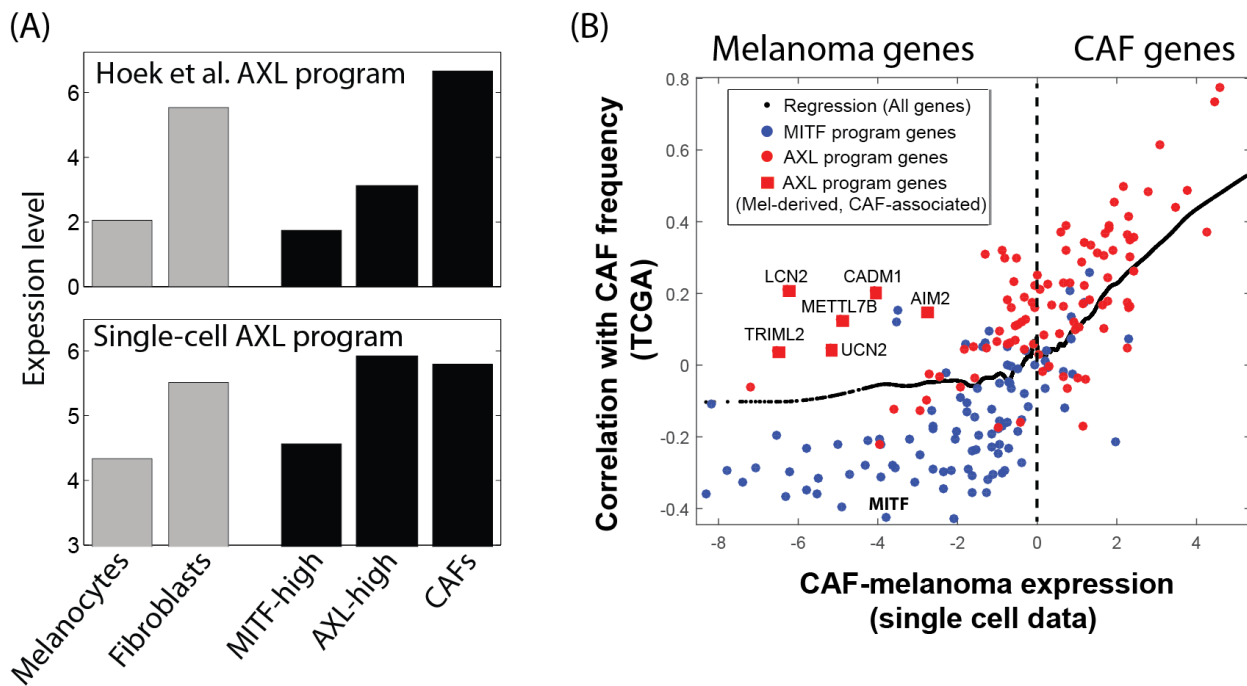


**Figure S14. Association between a malignant AXL program and CAFs.** **(A)** Average expression ( $\log_2(\text{TPM}+1)$ ) of the AXL program (Y-axis) as defined here (bottom) and by Hoek et al. (top, ref. 30) in CAFs and melanoma cells from our tumors (this work, black bars) and in foreskin melanocytes and primary fibroblasts from the Roadmap Epigenome project (grey bars). Melanoma cells were partitioned to those from AXL-high and MITF-high tumors as marked in Fig. 3A. **(B)** CAF expression correlates with higher AXL program than MITF program expression in melanoma malignant cells. Scatter plot shows for each gene (dot) from the MITF (blue) or AXL (red) programs (as defined based on single-cell transcriptomes) the correlation of its expression with inferred CAF frequency across bulk tumors (Y-axis, from TCGA transcriptomes), and how specific its expression is to CAFs vs. melanoma malignant cells (X-axis, based on single-cell transcriptomes). Black dots indicate the expected correlations at each value of the horizontal axis as defined by a LOWESS regression over all genes. The average correlation values of MITF program genes are significantly lower than those of all genes and the correlation values of AXL program genes are significantly higher than those of all genes, even after restricting the analysis to melanoma-specific genes (X-axis < -2,  $P < 0.01$ , t-test). A subset of AXL-program genes are specifically expressed in melanoma cells (but not CAFs) based on the single cell expression profiles, but associated with CAF abundance in bulk tumors (marked by red squares and gene names). MITF is negatively correlated with CAF abundance ( $R = -0.42$ ) and is also indicated by gene name.

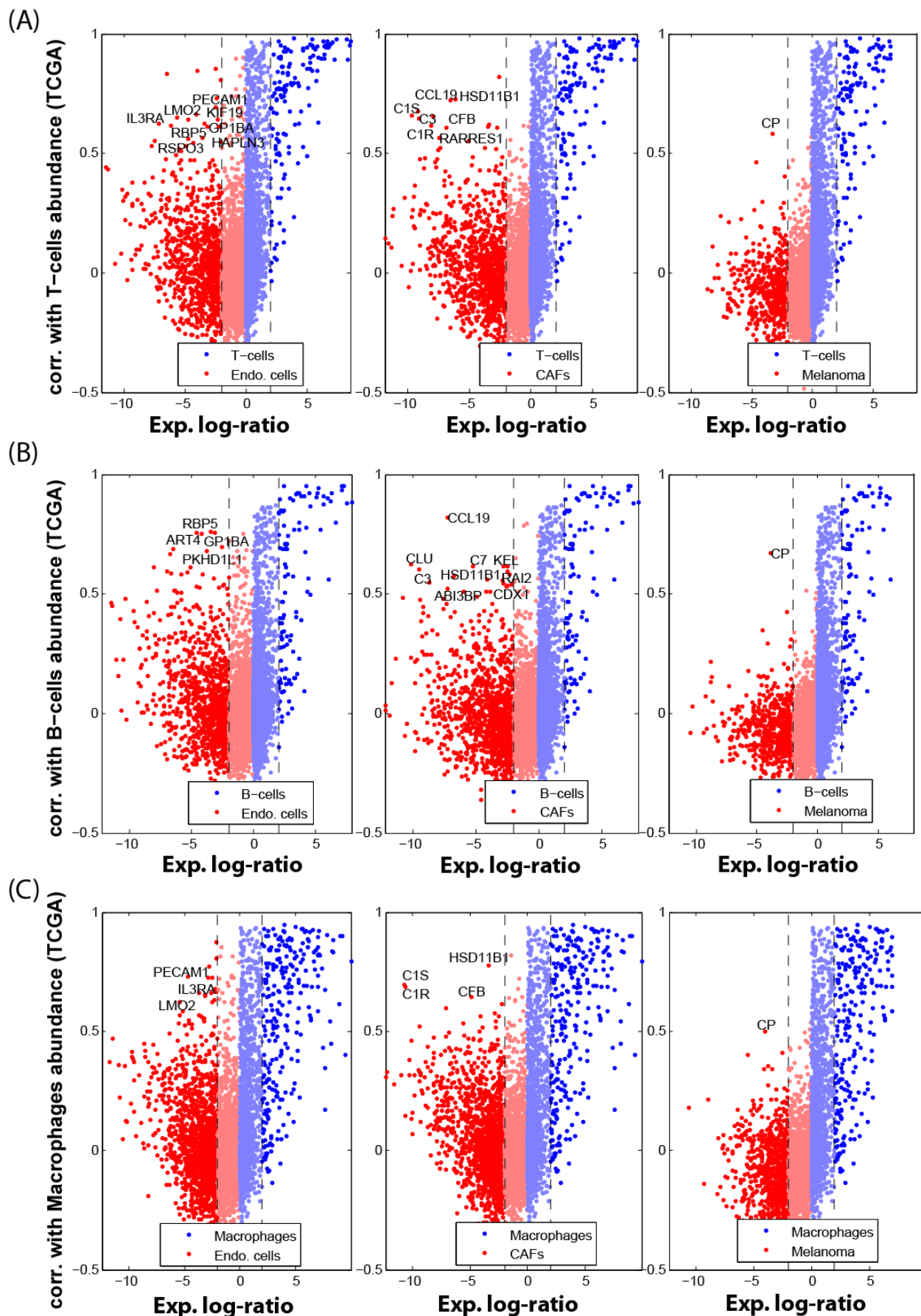


**Figure S15. Identification of putative genes underlying cell-to-cell interactions from analysis of single cell profiles and TCGA samples.** We searched for genes that underlie potential cell-to-cell interactions, defined as those that are primarily expressed by cell type  $M$  (as defined by the single cell data) but correlate with the inferred relative frequency of cell type  $N$  (as defined from correlations across TCGA samples). For each pair of cell types ( $M$  and  $N$ ), we restricted the analysis to genes that are at least four-fold higher in cell type  $M$  than in cell type  $N$  and in any of the other four cell types. We then calculated the Pearson correlation coefficient ( $R$ ) between the expression of each of these genes in TCGA samples and the relative frequency of cell type  $N$  in those samples, and converted these into  $Z$ -scores. The set of genes with  $Z > 3$  and a correlation above 0.5 was defined as potential candidates that mediate an interaction between cell type  $M$  and cell type  $N$ . **(A)** Of all the pairwise comparisons we identified interactions only between immune cells (B, T, macrophages) and non-immune cells (CAFs, endothelial cells, malignant melanoma) cells, such that the expression of genes from non-immune cells correlated with the relative frequency of immune cell types. Each plot shows a single pairwise comparison ( $M$  vs.  $N$ ), including interactions of non-immune cell types (endothelial cells: left; CAFs: middle; malignant melanoma: right) with each of T-cells (A), B-cells (**B**) and macrophages (**C**). Each plot compares for each gene (dot) the relative expression of genes in the two cell types being compared ( $M-N$ ) and the correlations of these genes' expression with the inferred frequency of cell type  $N$  across bulk TCGA tumors. Dashed lines denote the four-fold threshold. Genes that may underlie potential interactions, as defined above, are highlighted.

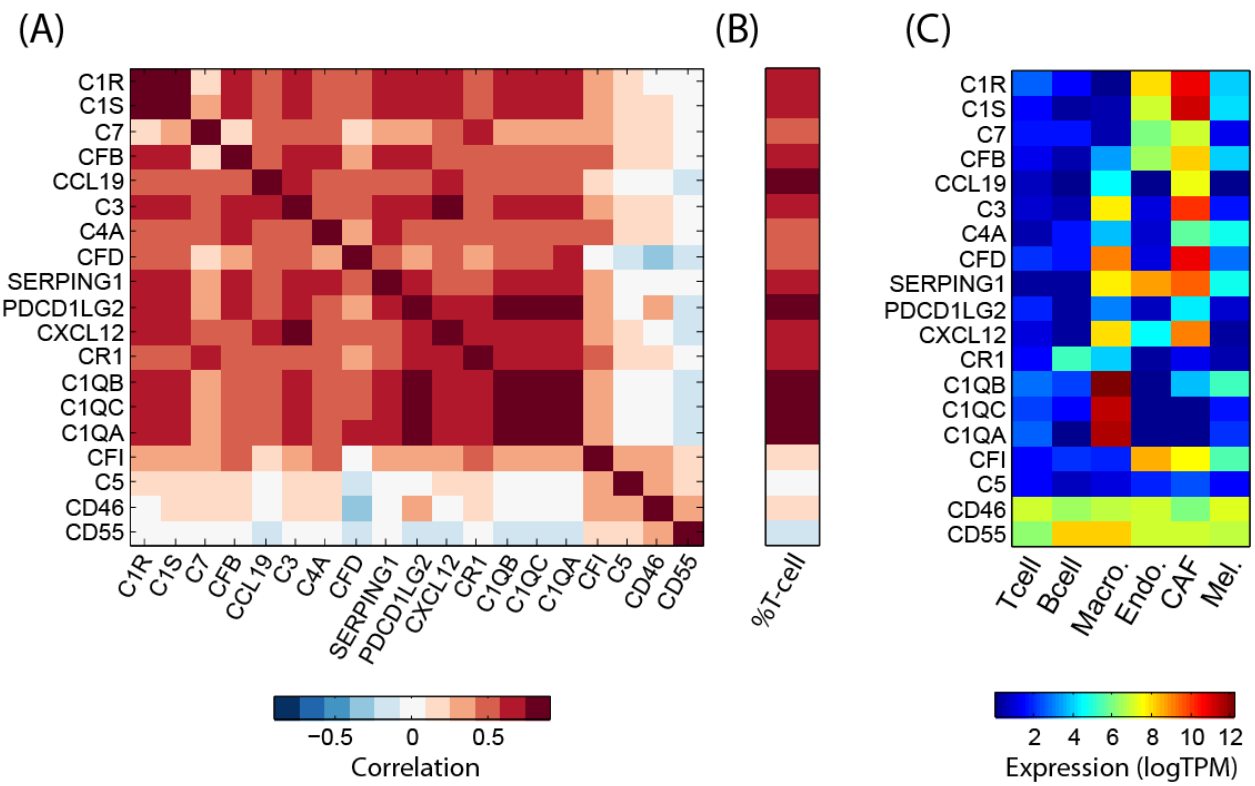


**Figure S16. Immune modulators expressed by CAFs and macrophages.** **(A)** Pearson correlation coefficient (color bar) across TCGA melanoma tumors between the expression level of each of the immune modulators shown in Fig. 4B and additional complement factors with significant expression levels. **(B)** Correlations across TCGA melanoma tumors between the expression level of the genes shown in (A) and the average expression levels of T cell marker genes. **(C)** Average expression level ( $\log_2(\text{TPM}+1)$ , color bar) of the genes shown in (A) in the single cell data, for cells classified into each of the major cell types we identified. These results show that most complement factors are correlated with one another and with the abundance of T cells, even though some are primarily expressed by CAFs (including C3) and others by macrophages. In contrast, two complement factors (CFI, C5) and the complement regulatory genes (CD46 and CD55) show a different expression pattern.

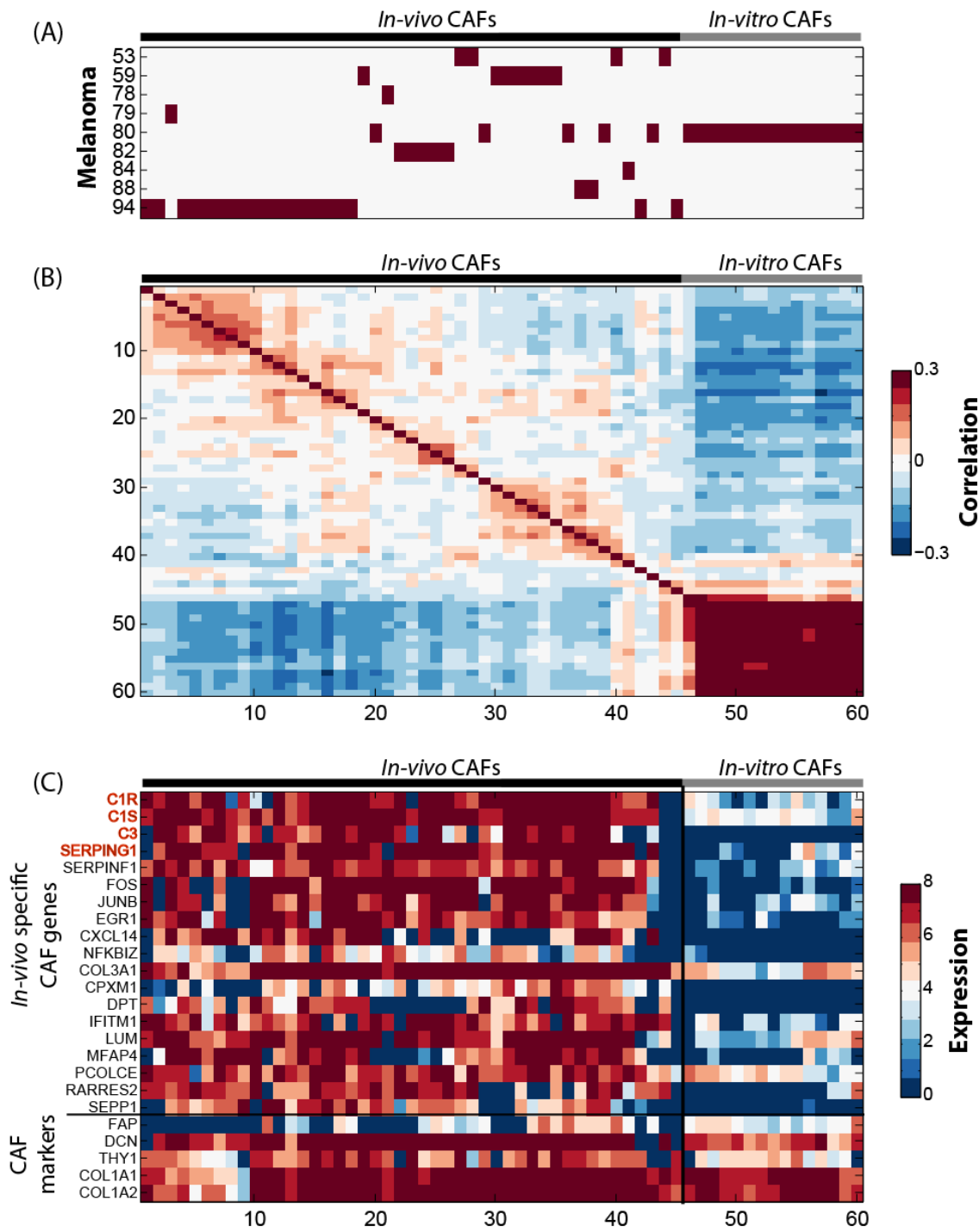


**Figure S17. Unique expression profiles of *in vivo* CAFs.** (A-B) Distinct expression profiles in *in vivo* and *in vitro* CAFs. Shown are Pearson correlation coefficient between individual CAFs isolated *in vivo* from seven melanoma tumors, and CAFs cultured from one tumor (melanoma 80). Hierarchical clustering shows two clusters, one consisting of all *in vivo* CAFs, regardless of their tumor-of-origin (marked in (A)), and another of the *in vitro* CAFs. (C) Unique markers of *in vivo* CAFs include putative cell-cell interaction candidates. Left: Heatmap shows the expression level ( $\log_2(\text{TPM}+1)$ ) of CAF markers (bottom) and the top 14 genes with higher expression in *in-vivo* compared to *in-vitro* CAFs ( $t$ -test). Right: average (bulk) expression of the genes in the *in-vivo* CAFs, *in-vitro* CAFs, and primary foreskin fibroblasts from the Roadmap Epigenome project. Potential interacting genes from Fig. 4B are highlighted in bold red.

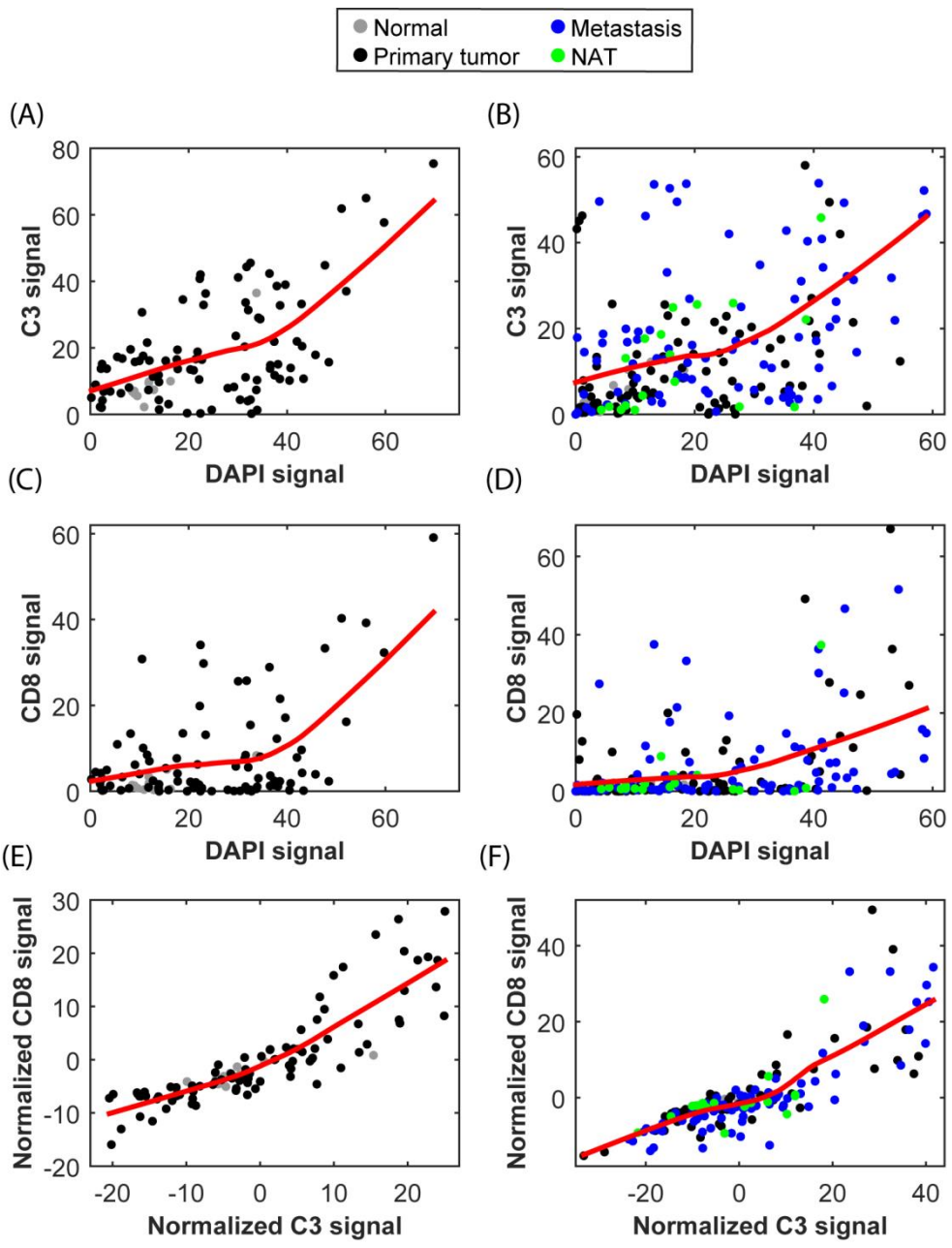


**Figure S18. TMA analysis of complement factor 3 association with CD8+ T-cell infiltration, and control staining.** Two TMAs (CC38-01 and ME208, shown in A, C, E and B, D, F, respectively) were used to evaluate the association between complement factor 3 (C3) and CD8 across a large number of tissues obtained by core biopsies of normal skin, primary tumors, metastatic lesions and NATs (normal skin with adjacent tumor). In both TMAs with a total of 308 core biopsies, we observed high correlation between C3 and CD8 ( $R > 0.8$ , shown in Fig. 4C for one TMA). To verify that this correlation is not due to technical effects in which some tissues stain more than others irrespective of the stains examined (e.g., due to variability in cellularity or tissue quality), we normalized the values (%area, Methods) for both C3 and CD8 by those of DAPI staining. Indeed, we found a non-random yet non-linear association between DAPI stains and either C3 (A, B), or CD8 (C, D), which were removed by subtracting a LOWESS regression, shown as red curves in panels A-D. The normalized C3 and CD8 values were not correlated with DAPI levels, yet maintained a high correlation with one another (E, F).  $R = 0.86$  and  $0.74$  for primary and normal skin in panel E (TMA CC38-01), and  $R = 0.78$ ,  $0.86$ ,  $0.63$  and  $0.31$  for primary melanomas, metastasis, NATs and normal skin in panel F (TMA ME208), respectively.

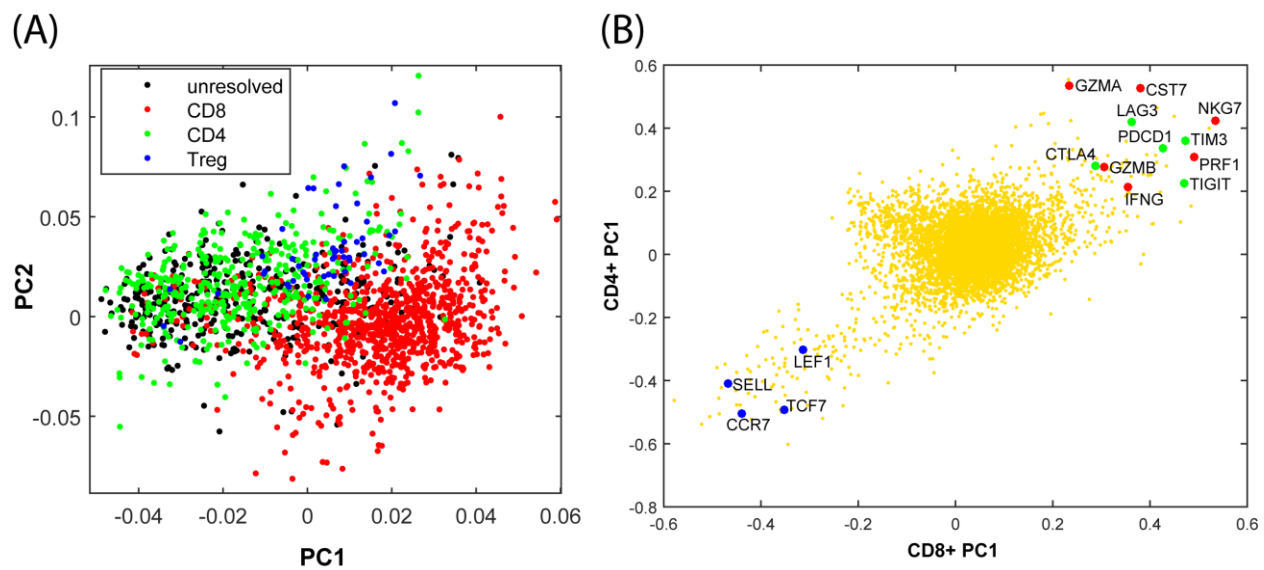


**Figure S19. Cytotoxic and naïve expression programs in T cells.** (A) Cell scores from a combined PCA of all T cells. Cells are colored as CD8+ (red), CD4+ (green), T-reg (blue) and unresolved (black) based on expression of marker genes (Fig. 5A, Methods). (B) Gene scores for PC1 from a PCA of CD8+ cells (x-axis) and PC2 from a PCA of CD4+ cells (Y-axis). Selected marker genes are highlighted, including genes known to be associated with cytotoxic/active (red), naïve (blue) and exhausted (green) T cell states.

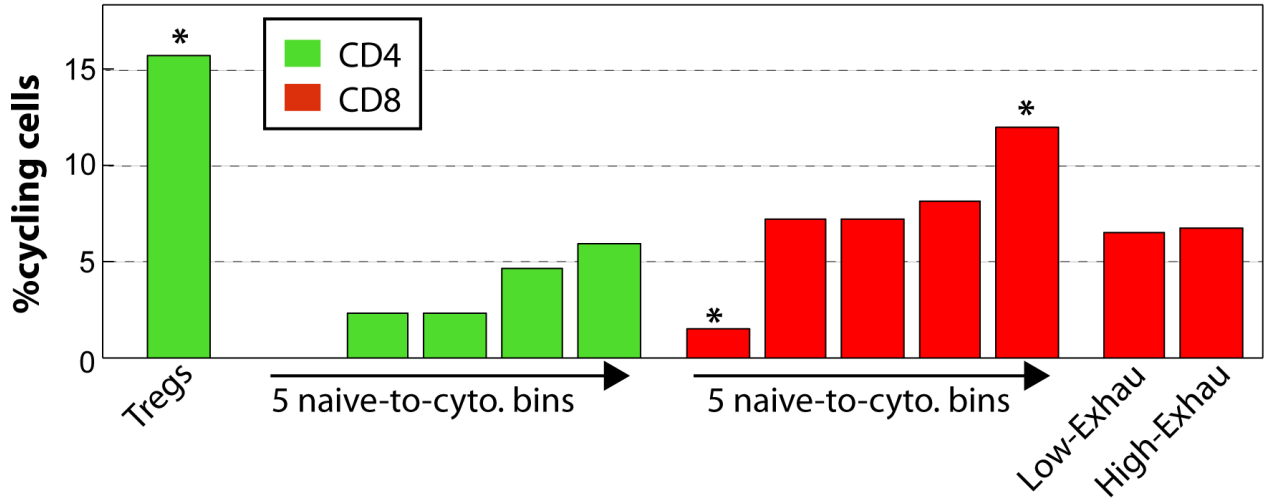


**Figure S20. Frequency of cycling cells in different subsets of T-cells.** Shown is the frequency of cycling T cells (as identified based on the expression of G1/S and G2/M gene-sets; **Methods**) for different subsets of T cells, including Tregs, CD4+ cells separated into five bins of increasing activation (arrow below green bars), CD8+ cells separated into five bins of increasing activation (arrow below red bars), and active/cytotoxic CD8+ further partitioned into those with relatively high or low exhaustion, as shown in Fig. 5D. Asterisks denote subsets with significant enrichment or depletion of cycling cells across all cells from the same subset of CD4+ or CD8+ cells as defined by  $P < 0.05$  in a hypergeometric test. Cell cycle frequency is associated with activation state of CD8+ T-cells, as the first bin is significantly depleted and the fifth bin is significantly enriched. A similar trend is observed in CD4+ T-cells (no cycling cells in the first bin and highest frequency in fifth bin), although none of the CD4 bins was significantly depleted or enriched. Exhaustion was not associated with significant differences in cell cycle frequency ( $P = 0.34$ , Chi-square test).

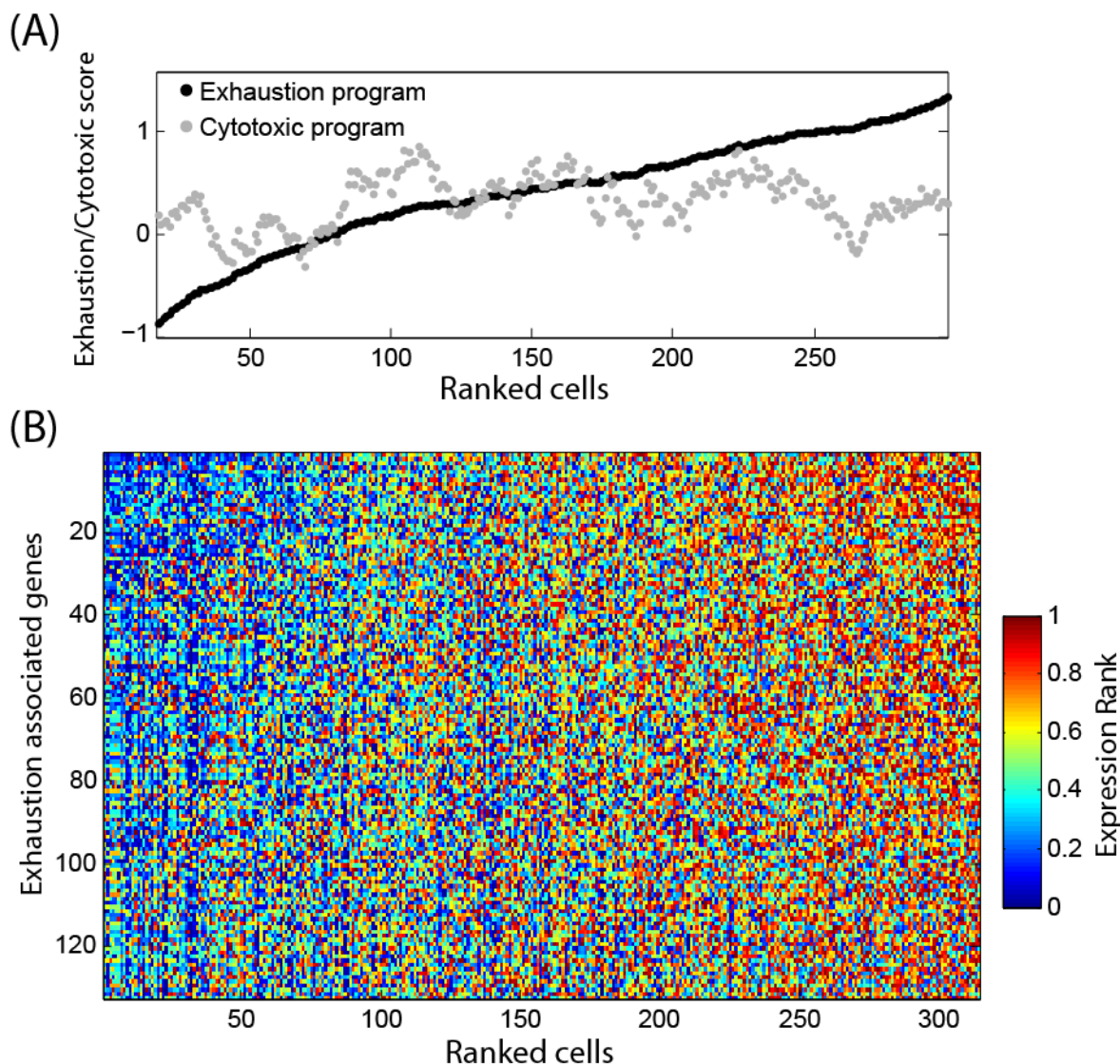


**Figure S21. Exhaustion program in Mel75.** PCA of 314 CD8 T-cells from Mel75 identified an exhaustion program in which the top scoring genes for PC1 included the five co-inhibitory receptors shown in Fig. 5B as well as additional exhaustion-associated genes (e.g., BTLA, CBLB). We defined PC1-associated genes based on a correlation  $p$ -value of 0.01 (with Bonferroni correction for multiple testing, see Table S13). Cells were then ranked by the residual between average expression of these PC1-associated genes (referred to as the exhaustion program) and average expression of the cytotoxic genes shown in Fig. 5B (referred to as the cytotoxic program) using a LOWESS regression, as shown in Fig. 5D. Finally, for each gene, we ranked its expression levels across the CD8 T-cells from Mel75 and converted these to rank scores between 0 and 1 such that the  $i$  highest-expressing cell received a rank score of  $i/314$ , where 314 represents the number of CD8 T cells from Mel75. **(A)** Exhaustion and cytotoxic program scores for ranked Mel75 CD8 T-cells, after applying a moving average with windows of 31 genes. **(B)** The heatmap shows expression ranks of PC1-associated genes across the CD8 T-cells from Mel75 cells, ranked as described above.

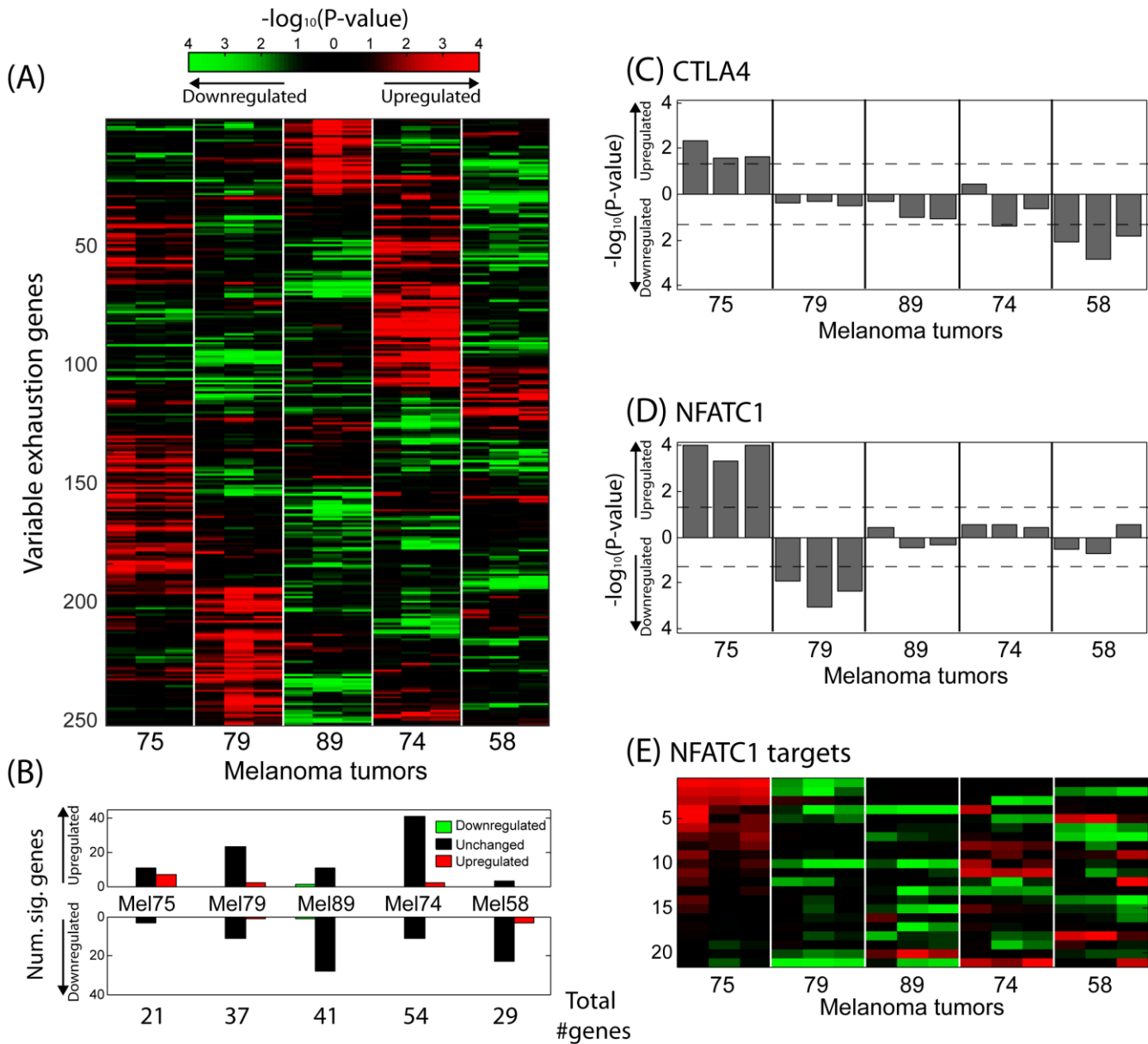


**Figure S22. Tumor-specific exhaustion programs.** **(A)** Heatmap shows the significance ( $-\log_{10}(P\text{-value})$ ) of tumor-specific variation in exhaustion gene scores (log-ratio in high vs. low exhaustion cells) comparing each tumor to all other tumors combined, for the same genes (and the same order) as shown in Fig. 5F. The sign of significance values reflects the direction of change (positive values shown in red reflect higher exhaustion values compared to other tumors while negative values shown in green reflect lower exhaustion values compared to other tumors). Three values are shown for each tumor, corresponding to exhaustion scores based on the exhaustion gene-sets derived from Mel75 analysis (Fig. S22), from Wherry et al. (46), and from Baitsch et al. (48) respectively. **(B)** Tumor-specific associations with the exhaustion program, detected by co-expression across single cells, are not detected by the overall (bulk) tumor-specific expression in CD8 T-cells. Genes with significant tumor-specific up- or down-regulation in high-exhaustion cells (FDR  $< 0.05$  in each tumor, based on median of the three exhaustion scores), were divided to three classes (bars) based on the differences in their overall expression level in CD8 T-cells among the different tumors (green: genes lower in the respective tumor by at least two fold. Red: genes higher in the respective tumor by at least two fold. Black: genes with less than two-fold difference). This demonstrates that most differences across tumors in exhaustion co-expression are in genes whose overall expression is similar in the different tumors and thus their distinct association with co-expression could not have been identified in bulk level analysis of the CD8 T-cells. **(C–D)** Bar plots showing the significance of tumor-specific variation, as in (A), for CTLA4 (C) and NFATC1 (D). Dashed lines indicate significance thresholds that correspond to  $P < 0.05$ . **(E)** Heatmap (as in subfigure A) for the target genes of NFATC1 (49).

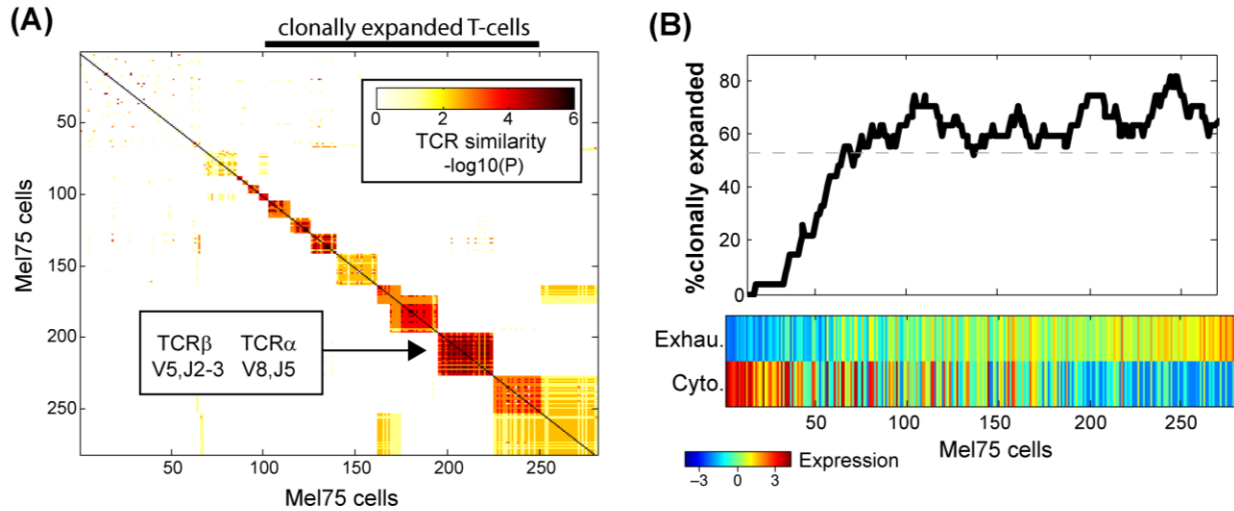


**Figure S23. Detection of Mel74 expanded T-cell clones by TCR sequence.** **(A)** Clustering of Mel75 cells by their TCR segment usage. TCR Similarity was defined as zero for any pair with at least one inconsistent allele (i.e. resolved in both cells but distinct among the two cells), and as  $-\log_{10}(P)$  for any pair without inconsistent alleles, where P reflects the estimated probability of randomly observing this or a higher degree of segment usage similarity. P is equal to the product of the probabilities for the four TCR segments,  $P(i,j)=P_{\beta\nu}(i,j)*P_{\beta\lvert}(i,j)*P_{\alpha\nu}(i,j)*P_{\alpha\lvert}(i,j)$ . For each segment, the probability equals one if segment usage is unresolved in at least one of the cells of the pair, and otherwise (i.e., if the two cells have the same allele) the probability is  $1/N$ , where N is the number of distinct alleles that were identified for that segment. The TCR usage of one exemplary cluster is indicated. **(B)** Mel75 cells were ordered by the average relative expression of Exhaustion and Cytotoxic genes, as shown in Fig. 5B, and the percentage of clonally expanded cells (i.e., belonging to the clusters indicated in A) is shown with a moving average of 20 cells, demonstrating the depletion of expanded T cells among cells with high cytotoxic and low exhaustion expression. Dashed line indicates the overall frequency of clonally expanded cells. Note that the top and bottom panels are aligned but that due to the use of a 20-cell moving average, the top panel can only start at the 11<sup>th</sup> cell and end at the 11<sup>th</sup> cell from the end.

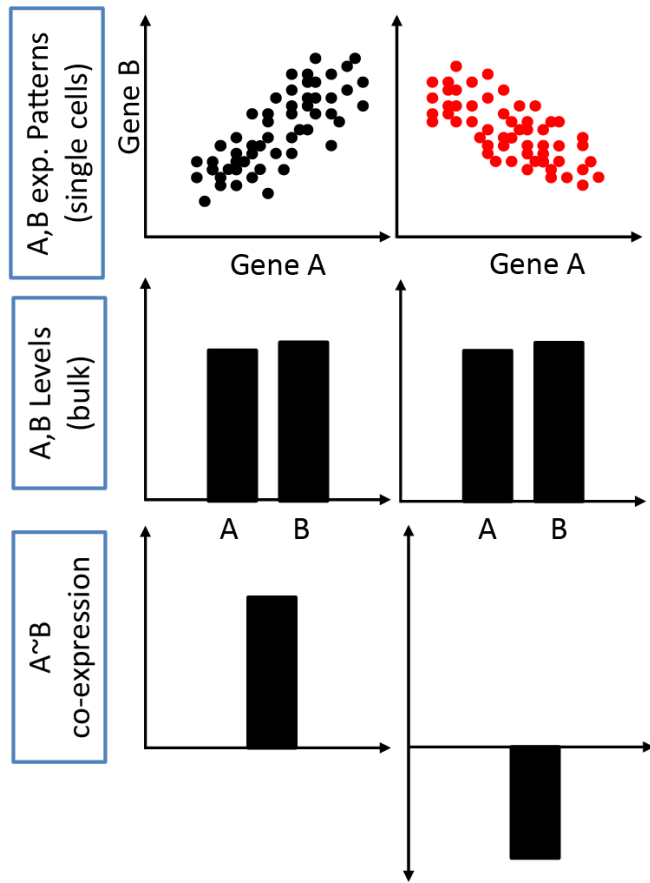


**Figure S24. Identification of distinct co-expression programs may require single cell analysis.**  
 Schematic depicting how single-cell RNA-seq can distinguish two scenarios that are indistinguishable by bulk profiling. Across individual tumor cells (top), genes A and B are either positively (left) or negatively (right) correlated. In bulk tumor (middle), the average expression of A,B cannot distinguish the two scenarios, whereas co-expression estimates from single cell RNA-seq (bottom) do so.

**Table S1. Characteristics of patients and samples included in this study**

Sample ID	Age/sex	Mutation status	Pre-operative treatment	Site of resection	Post-op. treatment	Alive/deceased
Melanoma_53	77/F	Wild-type	None	Subcutaneous back lesion	None	Alive
Melanoma_58	67/F	Wild-type	Ipilimumab	Subcutaneous leg lesion	None	Alive
Melanoma_59	80/M	Wild-type	None	Femoral lymph node	Nivolumab.	Deceased
Melanoma_60	69/M	BRAF V600K	Trametinib, ipilimumab	Spleen	None	Alive
Melanoma_65	65/M	BRAF V600E	None	Paraspinal intramuscular	Neovax	Alive
Melanoma_67	58/M	BRAF V600E	None	Axillary lymph node	None	Alive
Melanoma_71	79/M	NRAS Q61L	None	Transverse colon	None	Alive
Melanoma_72	57/F	NRAS Q61R	IL-2, nivolumab, ipilimumab + anti-KIR-Ab	External iliac lymph node	None	Alive
Melanoma_74	63/M	n/a	Nivolumab	Terminal ileum	None	Alive
Melanoma_75	80/M	Wild-type	Ipilimumab + nivolumab, WDVAX, WDVAX,	Subcutaneous leg lesion	Nivolumab	Alive
Melanoma_78	73/M	NRAS Q61L	ipilimumab + nivolumab	Small bowel	None	Deceased
Melanoma_79	74/M	Wild-type	None	Axillary lymph node	None	Alive
Melanoma_80	86/F	NRAS Q61L	None	Axillary lymph node	None	Alive
Melanoma_81	43/F	BRAF V600E	None	Axillary lymph node	None	Alive
Melanoma_82	81/M	Wild-type	None	Axillary lymph node	None	Alive
Melanoma_84	67/M	Wild-type	None	Acral primary	None	Alive
Melanoma_88	54/F	NRAS Q61L	Tremelimumab + MEDI3617	Cutanoues met	None	Alive
Melanoma_89	67/M	n/a	None	Axillary lymph node	None	Alive
Melanoma_94	54/F	Wild-type	IFN, ipilimumab + nivolumab	Iliac lymph node	None	Alive

**Table S2. Number of cells classified to each cell type in each tumor.** (Provided as a separate file.)

**Table S3. Cell type specific genes.** (Provided as a separate file.)

**Table S4. PCA. The top 50 correlated genes and the top MsigDB enrichments of those genes for the first six PCs.** (Provided as a separate file.)

**Table S5. Core signature of cell cycle genes expressed in cycling malignant cells from both low-cycling and high-cycling tumors.** (Provided as a separate file.)

**Table S6. Differentially regulated genes in Region 1.** (Provided as a separate file.)

**Table S7. List of genes included in the MITF-program.** (Provided as a separate file.)

**Table S8. List of genes included in the AXL-program.** (Provided as a separate file.)

**Table S9. Expression data for pre-treatment and post-relapse samples.** (Provided as a separate file.)

**Table S10. Sample information on pre-treatment and post-relapse samples (ref. 12)**

Patient ID	Treatment	Best response (in % by RECIST criteria)	PFS (months)
1	Dabrafenib/Trametinib	-100 (CR)	18
2	Dabrafenib /Trametinib	-20 (SD)	10
3	Vemurafenib	-51 (PR)	5
4	Dabrafenib /Trametinib	-42 (PR)	3
5	Dabrafenib /Trametinib	-53 (PR)	2
6	Dabrafenib /Trametinib	-23 (SD)	2

CR = complete response, PR = partial response, SD = stable disease, PFS = progression-free survival, RECIST = Response Evaluation Criteria In Solid Tumors (67).

**Table S11. Characteristics of examined cell lines**

Cell line	MITF mRNA expression	AXL mRNA expression	Vemurafenib (IC50 $\mu$ M)	Response to BRAF-inhibition	BRAF mutation	AXL expressing cells (%)
IGR39	7.65	10.77	8	Resistant	BRAF V600E	98
LOXIMVI	5.68	10.43	8	Resistant	BRAF V600E / I208V	97
WM793	6.39	10.05	8	Resistant	BRAF V600E	99
RPMI-7951	6.2	9.78	8	Resistant	BRAF V600E	98
SKMEL24	7.36	9.74	5.15	Resistant	BRAF V600E	98
A2058	8.71	9.63	8	Resistant	BRAF V600E	93
Hs294T	8.89	8.81	8	Resistant	BRAF V600E	93
WM115	6.85	8.29	8	Resistant	BRAF V600D	94
IPC298	10.55	5.9	8	Resistant	NRAS Q61L NRAS Q61K/ BRAF D287H/ E275K	24
SKMEL30	10.87	5.34	8	Resistant	E275K	1
A375	7.64	9.33	0.26	Sensitive	BRAF V600E	96
WM2664	10.43	8.19	1.58	Sensitive	BRAF V600D	98
WM88	10.05	6.39	0.2	Sensitive	BRAF V600E	1
UACC62	9.5	5.85	0.25	Sensitive	BRAF V600E	2
MELHO	11.15	4.87	0.31	Sensitive	BRAF V600E	1
SKMEL28	10.92	4.87		Sensitive	BRAF V600E	3
Colo679	10.34	4.83	0.55	Sensitive	BRAF V600E	0
IGR37	10.85	4.73	0.9	Sensitive	BRAF V600E	1

MITF mRNA and AXL mRNA, vemurafenib IC50s and mutational status were extracted from CCLE (35). Cells were analyzed for the fraction of AXL-high cells using FACS. Cell lines highlighted in gray were subsequently used for treatment experiments and measurement of AXL-high fractions by flow-cytometry and multiplexed quantitative single-cell immunofluorescence analysis. Cell lines that are highlighted in gray were used for subsequent drug treatment experiments, flow-cytometry and single-cell immunofluorescence analysis.

**Table S12. List of genes preferentially expressed in Tregs.** (Provided as a separate file.)**Table S13. Genes associated with Mel75 exhaustion signature.** (Provided as a separate file.)**Table S14. Association of genes with exhaustion signature across five tumors.** (Provided as a separate file.)**Table S15. CAF-derived genes that correlate with the abundance of T-cells.** (Provided as a separate file.)**Table S16. Curated list of housekeeping genes used for QC.** (Provided as a separate file.)

## References and Notes

1. D. Hanahan, R. A. Weinberg, Hallmarks of cancer: The next generation. *Cell* **144**, 646–674 (2011). [Medline doi:10.1016/j.cell.2011.02.013](#)
2. C. E. Meacham, S. J. Morrison, Tumour heterogeneity and cancer cell plasticity. *Nature* **501**, 328–337 (2013). [Medline doi:10.1038/nature12624](#)
3. F. S. Hodi, S. J. O'Day, D. F. McDermott, R. W. Weber, J. A. Sosman, J. B. Haanen, R. Gonzalez, C. Robert, D. Schadendorf, J. C. Hassel, W. Akerley, A. J. van den Eertwegh, J. Lutzky, P. Lorigan, J. M. Vaubel, G. P. Linette, D. Hogg, C. H. Ottensmeier, C. Lebbé, C. Peschel, I. Quirt, J. I. Clark, J. D. Wolchok, J. S. Weber, J. Tian, M. J. Yellin, G. M. Nichol, A. Hoos, W. J. Urba, Improved survival with ipilimumab in patients with metastatic melanoma. *N. Engl. J. Med.* **363**, 711–723 (2010). [Medline](#)
4. J. R. Brahmer, C. G. Drake, I. Wollner, J. D. Powderly, J. Picus, W. H. Sharfman, E. Stankevich, A. Pons, T. M. Salay, T. L. McMiller, M. M. Gilson, C. Wang, M. Selby, J. M. Taube, R. Anders, L. Chen, A. J. Korman, D. M. Pardoll, I. Lowy, S. L. Topalian, Phase I study of single-agent anti-programmed death-1 (MDX-1106) in refractory solid tumors: Safety, clinical activity, pharmacodynamics, and immunologic correlates. *J. Clin. Oncol.* **28**, 3167–3175 (2010). [Medline doi:10.1200/JCO.2009.26.7609](#)
5. J. R. Brahmer, S. S. Tykodi, L. Q. Chow, W. J. Hwu, S. L. Topalian, P. Hwu, C. G. Drake, L. H. Camacho, J. Kauh, K. Odunsi, H. C. Pitot, O. Hamid, S. Bhatia, R. Martins, K. Eaton, S. Chen, T. M. Salay, S. Alaparthy, J. F. Gross, A. J. Korman, S. M. Parker, S. Agrawal, S. M. Goldberg, D. M. Pardoll, A. Gupta, J. M. Wigginton, Safety and activity of anti-PD-L1 antibody in patients with advanced cancer. *N. Engl. J. Med.* **366**, 2455–2465 (2012). [Medline doi:10.1056/NEJMoa1200694](#)
6. S. L. Topalian, F. S. Hodi, J. R. Brahmer, S. N. Gettinger, D. C. Smith, D. F. McDermott, J. D. Powderly, R. D. Carvajal, J. A. Sosman, M. B. Atkins, P. D. Leming, D. R. Spigel, S. J. Antonia, L. Horn, C. G. Drake, D. M. Pardoll, L. Chen, W. H. Sharfman, R. A. Anders, J. M. Taube, T. L. McMiller, H. Xu, A. J. Korman, M. Jure-Kunkel, S. Agrawal, D. McDonald, G. D. Kollia, A. Gupta, J. M. Wigginton, M. Sznol, Safety, activity, and immune correlates of anti-PD-1 antibody in cancer. *N. Engl. J. Med.* **366**, 2443–2454 (2012). [Medline doi:10.1056/NEJMoa1200690](#)
7. O. Hamid, C. Robert, A. Daud, F. S. Hodi, W. J. Hwu, R. Kefford, J. D. Wolchok, P. Hersey, R. W. Joseph, J. S. Weber, R. Dronca, T. C. Gangadhar, A. Patnaik, H. Zarour, A. M. Joshua, K. Gergich, J. Elassaiss-Schaap, A. Algazi, C. Mateus, P. Boasberg, P. C. Tumeh, B. Chmielowski, S. W. Ebbinghaus, X. N. Li, S. P. Kang, A. Ribas, Safety and tumor responses with lambrolizumab (anti-PD-1) in melanoma. *N. Engl. J. Med.* **369**, 134–144 (2013). [Medline doi:10.1056/NEJMoa1305133](#)
8. J. S. Weber, R. R. Kudchadkar, B. Yu, D. Gallenstein, C. E. Horak, H. D. Inzunza, X. Zhao, A. J. Martinez, W. Wang, G. Gibney, J. Kroeger, C. Eysmans, A. A. Sarnaik, Y. A. Chen, Safety, efficacy, and biomarkers of nivolumab with vaccine in ipilimumab-refractory or -naive melanoma. *J. Clin. Oncol.* **31**, 4311–4318 (2013). [Medline doi:10.1200/JCO.2013.51.4802](#)

9. K. M. Mahoney, M. B. Atkins, Prognostic and predictive markers for the new immunotherapies. *Oncology* **28** (suppl. 3), 39–48 (2014). [Medline](#)
10. J. Larkin, V. Chiarion-Sileni, R. Gonzalez, J. J. Grob, C. L. Cowey, C. D. Lao, D. Schadendorf, R. Dummer, M. Smylie, P. Rutkowski, P. F. Ferrucci, A. Hill, J. Wagstaff, M. S. Carlino, J. B. Haanen, M. Maio, I. Marquez-Rodas, G. A. McArthur, P. A. Ascierto, G. V. Long, M. K. Callahan, M. A. Postow, K. Grossmann, M. Sznol, B. Dreno, L. Bastholt, A. Yang, L. M. Rollin, C. Horak, F. S. Hodi, J. D. Wolchok, Combined nivolumab and ipilimumab or monotherapy in untreated melanoma. *N. Engl. J. Med.* **373**, 23–34 (2015). [Medline](#)
11. A. Snyder, V. Makarov, T. Merghoub, J. Yuan, J. M. Zaretsky, A. Desrichard, L. A. Walsh, M. A. Postow, P. Wong, T. S. Ho, T. J. Hollmann, C. Bruggeman, K. Kannan, Y. Li, C. Elipenahli, C. Liu, C. T. Harbison, L. Wang, A. Ribas, J. D. Wolchok, T. A. Chan, Genetic basis for clinical response to CTLA-4 blockade in melanoma. *N. Engl. J. Med.* **371**, 2189–2199 (2014). [Medline doi:10.1056/NEJMoa1406498](#)
12. N. Wagle, C. Emery, M. F. Berger, M. J. Davis, A. Sawyer, P. Pochanard, S. M. Kehoe, C. M. Johannessen, L. E. Macconail, W. C. Hahn, M. Meyerson, L. A. Garraway, Dissecting therapeutic resistance to RAF inhibition in melanoma by tumor genomic profiling. *J. Clin. Oncol.* **29**, 3085–3096 (2011). [Medline doi:10.1200/JCO.2010.33.2312](#)
13. E. M. Van Allen, N. Wagle, A. Sucker, D. J. Treacy, C. M. Johannessen, E. M. Goetz, C. S. Place, A. Taylor-Weiner, S. Whittaker, G. V. Kryukov, E. Hodis, M. Rosenberg, A. McKenna, K. Cibulskis, D. Farlow, L. Zimmer, U. Hillen, R. Gutzmer, S. M. Goldinger, S. Uigurel, H. J. Gogas, F. Egberts, C. Berking, U. Trefzer, C. Loquai, B. Weide, J. C. Hassel, S. B. Gabriel, S. L. Carter, G. Getz, L. A. Garraway, D. Schadendorf; Dermatologic Cooperative Oncology Group of Germany (DeCOG), The genetic landscape of clinical resistance to RAF inhibition in metastatic melanoma. *Cancer Discov.* **4**, 94–109 (2014). [Medline doi:10.1158/2159-8290.CD-13-0617](#)
14. A. K. Shalek, R. Satija, X. Adiconis, R. S. Gertner, J. T. Gaublomme, R. Raychowdhury, S. Schwartz, N. Yosef, C. Malboeuf, D. Lu, J. J. Trombetta, D. Gennert, A. Gnirke, A. Goren, N. Hacohen, J. Z. Levin, H. Park, A. Regev, Single-cell transcriptomics reveals bimodality in expression and splicing in immune cells. *Nature* **498**, 236–240 (2013). [Medline doi:10.1038/nature12172](#)
15. A. P. Patel, I. Tirosh, J. J. Trombetta, A. K. Shalek, S. M. Gillespie, H. Wakimoto, D. P. Cahill, B. V. Nahed, W. T. Curry, R. L. Martuza, D. N. Louis, O. Rozenblatt-Rosen, M. L. Suvà, A. Regev, B. E. Bernstein, Single-cell RNA-seq highlights intratumoral heterogeneity in primary glioblastoma. *Science* **344**, 1396–1401 (2014). [Medline doi:10.1126/science.1254257](#)
16. E. Z. Macosko, A. Basu, R. Satija, J. Nemesh, K. Shekhar, M. Goldman, I. Tirosh, A. R. Bialas, N. Kamitaki, E. M. Martersteck, J. J. Trombetta, D. A. Weitz, J. R. Sanes, A. K. Shalek, A. Regev, S. A. McCarroll, Highly parallel genome-wide expression profiling of individual cells using nanoliter droplets. *Cell* **161**, 1202–1214 (2015). [Medline doi:10.1016/j.cell.2015.05.002](#)
17. Materials and methods are available as supplementary materials on *Science* Online.
18. L. van der Maaten, G. Hinton, Visualizing data using t-SNE. *Nature* **9**, 2579–2605 (2008).

19. M. Ester, H.-P. Kriegel, J. Sander, X. Xu, “A density-based algorithm for discovering clusters in large spatial databases with noise,” in *Proceedings of the 2nd International Conference on Knowledge Discovery and Data Mining (KDD’96)* (AAAI Press, 1996), pp. 226–231.
20. M. L. Whitfield, G. Sherlock, A. J. Saldanha, J. I. Murray, C. A. Ball, K. E. Alexander, J. C. Matese, C. M. Perou, M. M. Hurt, P. O. Brown, D. Botstein, Identification of genes periodically expressed in the human cell cycle and their expression in tumors. *Mol. Biol. Cell* **13**, 1977–2000 (2002). [Medline](#)
21. A. Roesch, M. Fukunaga-Kalabis, E. C. Schmidt, S. E. Zabierowski, P. A. Brafford, A. Vultur, D. Basu, P. Gimotty, T. Vogt, M. Herlyn, A temporarily distinct subpopulation of slow-cycling melanoma cells is required for continuous tumor growth. *Cell* **141**, 583–594 (2010). [Medline doi:10.1016/j.cell.2010.04.020](#)
22. G. Shapiro *et al.*, “A first-in-human phase I study of the CDK4/6 inhibitor, LY2835219, for patients with advanced cancer,” presented at the *2013 American Society of Clinical Oncology (ASCO) Annual Meeting* (ASCO, 2013), abstr. 2500; available at <http://meetinglibrary.asco.org/content/111069-132>.
23. The Cancer Genome Atlas Network, Genomic classification of cutaneous melanoma. *Cell* **161**, 1681–1696 (2015). [Medline doi:10.1016/j.cell.2015.05.044](#)
24. C. M. Johannessen, L. A. Johnson, F. Piccioni, A. Townes, D. T. Frederick, M. K. Donahue, R. Narayan, K. T. Flaherty, J. A. Wargo, D. E. Root, L. A. Garraway, A melanocyte lineage program confers resistance to MAP kinase pathway inhibition. *Nature* **504**, 138–142 (2013). [Medline doi:10.1038/nature12688](#)
25. D. J. Konieczkowski, C. M. Johannessen, O. Abudayyeh, J. W. Kim, Z. A. Cooper, A. Piris, D. T. Frederick, M. Barzily-Rokni, R. Straussman, R. Haq, D. E. Fisher, J. P. Mesirov, W. C. Hahn, K. T. Flaherty, J. A. Wargo, P. Tamayo, L. A. Garraway, A melanoma cell state distinction influences sensitivity to MAPK pathway inhibitors. *Cancer Discov.* **4**, 816–827 (2014). [Medline doi:10.1158/2159-8290.CD-13-0424](#)
26. L. A. Garraway, H. R. Widlund, M. A. Rubin, G. Getz, A. J. Berger, S. Ramaswamy, R. Beroukhim, D. A. Milner, S. R. Granter, J. Du, C. Lee, S. N. Wagner, C. Li, T. R. Golub, D. L. Rimm, M. L. Meyerson, D. E. Fisher, W. R. Sellers, Integrative genomic analyses identify MITF as a lineage survival oncogene amplified in malignant melanoma. *Nature* **436**, 117–122 (2005). [Medline doi:10.1038/nature03664](#)
27. Z. Zhang, J. C. Lee, L. Lin, V. Olivas, V. Au, T. LaFramboise, M. Abdel-Rahman, X. Wang, A. D. Levine, J. K. Rho, Y. J. Choi, C. M. Choi, S. W. Kim, S. J. Jang, Y. S. Park, W. S. Kim, D. H. Lee, J. S. Lee, V. A. Miller, M. Arcila, M. Ladanyi, P. Moonsamy, C. Sawyers, T. J. Boggon, P. C. Ma, C. Costa, M. Taron, R. Rosell, B. Halmos, T. G. Bivona, Activation of the AXL kinase causes resistance to EGFR-targeted therapy in lung cancer. *Nat. Genet.* **44**, 852–860 (2012). [Medline](#)
28. X. Wu, X. Liu, S. Koul, C. Y. Lee, Z. Zhang, B. Halmos, AXL kinase as a novel target for cancer therapy. *Oncotarget* **5**, 9546–9563 (2014). [Medline doi:10.18632/oncotarget.2542](#)
29. A. D. Boiko, O. V. Razorenova, M. van de Rijn, S. M. Swetter, D. L. Johnson, D. P. Ly, P. D. Butler, G. P. Yang, B. Joshua, M. J. Kaplan, M. T. Longaker, I. L. Weissman, Human

melanoma-initiating cells express neural crest nerve growth factor receptor CD271. *Nature* **466**, 133–137 (2010). [Medline doi:10.1038/nature09161](#)

30. K. S. Hoek, O. M. Eichhoff, N. C. Schlegel, U. Döbbeling, N. Kobert, L. Schaerer, S. Hemmi, R. Dummer, In vivo switching of human melanoma cells between proliferative and invasive states. *Cancer Res.* **68**, 650–656 (2008). [Medline doi:10.1158/0008-5472.CAN-07-2491](#)
31. J. Müller, O. Krijgsman, J. Tsoi, L. Robert, W. Hugo, C. Song, X. Kong, P. A. Possik, P. D. Cornelissen-Steijger, M. H. Foppen, K. Kemper, C. R. Goding, U. McDermott, C. Blank, J. Haanen, T. G. Graeber, A. Ribas, R. S. Lo, D. S. Peeper, Low MITF/AXL ratio predicts early resistance to multiple targeted drugs in melanoma. *Nat. Commun.* **5**, 5712 (2014). [Medline doi:10.1038/ncomms6712](#)
32. F. Z. Li, A. S. Dhillon, R. L. Anderson, G. McArthur, P. T. Ferrao, Phenotype switching in melanoma: Implications for progression and therapy. *Front. Oncol.* **5**, 31 (2015). [Medline doi:10.3389/fonc.2015.00031](#)
33. W. Hugo, H. Shi, L. Sun, M. Piva, C. Song, X. Kong, G. Moriceau, A. Hong, K. B. Dahlman, D. B. Johnson, J. A. Sosman, A. Ribas, R. S. Lo, Non-genomic and Immune evolution of melanoma acquiring MAPKi resistance. *Cell* **162**, 1271–1285 (2015). [Medline doi:10.1016/j.cell.2015.07.061](#)
34. R. Nazarian, H. Shi, Q. Wang, X. Kong, R. C. Koya, H. Lee, Z. Chen, M. K. Lee, N. Attar, H. Sazegar, T. Chodon, S. F. Nelson, G. McArthur, J. A. Sosman, A. Ribas, R. S. Lo, Melanomas acquire resistance to B-RAF(V600E) inhibition by RTK or N-RAS upregulation. *Nature* **468**, 973–977 (2010). [Medline doi:10.1038/nature09626](#)
35. J. Barretina, G. Caponigro, N. Stransky, K. Venkatesan, A. A. Margolin, S. Kim, C. J. Wilson, J. Lehár, G. V. Kryukov, D. Sonkin, A. Reddy, M. Liu, L. Murray, M. F. Berger, J. E. Monahan, P. Morais, J. Meltzer, A. Korejwa, J. Jané-Valbuena, F. A. Mapa, J. Thibault, E. Bric-Furlong, P. Raman, A. Shipway, I. H. Engels, J. Cheng, G. K. Yu, J. Yu, P. Aspasia Jr., M. de Silva, K. Jagtap, M. D. Jones, L. Wang, C. Hatton, E. Palescandolo, S. Gupta, S. Mahan, C. Sougnez, R. C. Onofrio, T. Liefeld, L. MacConaill, W. Winckler, M. Reich, N. Li, J. P. Mesirov, S. B. Gabriel, G. Getz, K. Ardlie, V. Chan, V. E. Myer, B. L. Weber, J. Porter, M. Warmuth, P. Finan, J. L. Harris, M. Meyerson, T. R. Golub, M. P. Morrissey, W. R. Sellers, R. Schlegel, L. A. Garraway, The Cancer Cell Line Encyclopedia enables predictive modelling of anticancer drug sensitivity. *Nature* **483**, 603–607 (2012). [Medline doi:10.1038/nature11003](#)
36. W. H. Fridman, F. Pagès, C. Sautès-Fridman, J. Galon, The immune contexture in human tumours: Impact on clinical outcome. *Nat. Rev. Cancer* **12**, 298–306 (2012). [Medline doi:10.1038/nrc3245](#)
37. S. L. Carter, K. Cibulskis, E. Helman, A. McKenna, H. Shen, T. Zack, P. W. Laird, R. C. Onofrio, W. Winckler, B. A. Weir, R. Beroukhim, D. Pellman, D. A. Levine, E. S. Lander, M. Meyerson, G. Getz, Absolute quantification of somatic DNA alterations in human cancer. *Nat. Biotechnol.* **30**, 413–421 (2012). [Medline doi:10.1038/nbt.2203](#)
38. A. Kundaje, W. Meuleman, J. Ernst, M. Bilenky, A. Yen, A. Heravi-Moussavi, P. Kheradpour, Z. Zhang, J. Wang, M. J. Ziller, V. Amin, J. W. Whitaker, M. D. Schultz, L. D. Ward, A. Sarkar, G. Quon, R. S. Sandstrom, M. L. Eaton, Y. C. Wu, A. R. Pfenning,

- X. Wang, M. Claussnitzer, Y. Liu, C. Coarfa, R. A. Harris, N. Shores, C. B. Epstein, E. Gjoneska, D. Leung, W. Xie, R. D. Hawkins, R. Lister, C. Hong, P. Gascard, A. J. Mungall, R. Moore, E. Chuah, A. Tam, T. K. Canfield, R. S. Hansen, R. Kaul, P. J. Sabo, M. S. Bansal, A. Carles, J. R. Dixon, K. H. Farh, S. Feizi, R. Karlic, A. R. Kim, A. Kulkarni, D. Li, R. Lowdon, G. Elliott, T. R. Mercer, S. J. Neph, V. Onuchic, P. Polak, N. Rajagopal, P. Ray, R. C. Sallari, K. T. Siebenthal, N. A. Sinnott-Armstrong, M. Stevens, R. E. Thurman, J. Wu, B. Zhang, X. Zhou, A. E. Beaudet, L. A. Boyer, P. L. De Jager, P. J. Farnham, S. J. Fisher, D. Haussler, S. J. Jones, W. Li, M. A. Marra, M. T. McManus, S. Sunyaev, J. A. Thomson, T. D. Tlsty, L. H. Tsai, W. Wang, R. A. Waterland, M. Q. Zhang, L. H. Chadwick, B. E. Bernstein, J. F. Costello, J. R. Ecker, M. Hirst, A. Meissner, A. Milosavljevic, B. Ren, J. A. Stamatoyannopoulos, T. Wang, M. Kellis; Roadmap Epigenomics Consortium, Integrative analysis of 111 reference human epigenomes. *Nature* **518**, 317–330 (2015). [Medline](#)
39. M. M. Markiewski, R. A. DeAngelis, F. Benencia, S. K. Ricklin-Lichtsteiner, A. Koutoulaki, C. Gerard, G. Coukos, J. D. Lambris, Modulation of the antitumor immune response by complement. *Nat. Immunol.* **9**, 1225–1235 (2008). [Medline](#) doi:10.1038/ni.1655
40. E. J. Wherry, T cell exhaustion. *Nat. Immunol.* **12**, 492–499 (2011). [Medline](#) doi:10.1038/ni.2035
41. L. Chen, D. B. Flies, Molecular mechanisms of T cell co-stimulation and co-inhibition. *Nat. Rev. Immunol.* **13**, 227–242 (2013). [Medline](#) doi:10.1038/nri3405
42. H. Borghaei, L. Paz-Ares, L. Horn, D. R. Spigel, M. Steins, N. E. Ready, L. Q. Chow, E. E. Vokes, E. Felip, E. Holgado, F. Barlesi, M. Kohlhäufel, O. Arrieta, M. A. Burgio, J. Fayette, H. Lena, E. Poddubskaya, D. E. Gerber, S. N. Gettinger, C. M. Rudin, N. Rizvi, L. Crinò, G. R. Blumenschein Jr., S. J. Antonia, C. Dorange, C. T. Harbison, F. Graf Finckenstein, J. R. Brahmer, Nivolumab versus docetaxel in advanced nonsquamous non-small-cell lung cancer. *N. Engl. J. Med.* **373**, 1627–1639 (2015). [Medline](#) doi:10.1056/NEJMoa1507643
43. R. J. Motzer, B. Escudier, D. F. McDermott, S. George, H. J. Hammers, S. Srinivas, S. S. Tykodi, J. A. Sosman, G. Procopio, E. R. Plimack, D. Castellano, T. K. Choueiri, H. Gurney, F. Donskov, P. Bono, J. Wagstaff, T. C. Gaurer, T. Ueda, Y. Tomita, F. A. Schutz, C. Kollmannsberger, J. Larkin, A. Ravaud, J. S. Simon, L. A. Xu, I. M. Waxman, P. Sharma; CheckMate 025 Investigators, Nivolumab versus everolimus in advanced renal-cell carcinoma. *N. Engl. J. Med.* **373**, 1803–1813 (2015). [Medline](#) doi:10.1056/NEJMoa1510665
44. N. A. Rizvi, M. D. Hellmann, A. Snyder, P. Kvistborg, V. Makarov, J. J. Havel, W. Lee, J. Yuan, P. Wong, T. S. Ho, M. L. Miller, N. Rekhtman, A. L. Moreira, F. Ibrahim, C. Bruggeman, B. Gasmi, R. Zappasodi, Y. Maeda, C. Sander, E. B. Garon, T. Merghoub, J. D. Wolchok, T. N. Schumacher, T. A. Chan, Mutational landscape determines sensitivity to PD-1 blockade in non–small cell lung cancer. *Science* **348**, 124–128 (2015). [Medline](#) doi:10.1126/science.aaa1348
45. E. M. Van Allen, D. Miao, B. Schilling, S. A. Shukla, C. Blank, L. Zimmer, A. Sucker, U. Hillen, M. H. Geukes Foppen, S. M. Goldinger, J. Utikal, J. C. Hassel, B. Weide, K. C. Kaehler, C. Loquai, P. Mohr, R. Gutzmer, R. Dummer, S. Gabriel, C. J. Wu, D.

Schadendorf, L. A. Garraway, Genomic correlates of response to CTLA-4 blockade in metastatic melanoma. *Science* **350**, 207–211 (2015). [Medline](#)  
[doi:10.1126/science.aad0095](#)

46. E. J. Wherry, S. J. Ha, S. M. Kaech, W. N. Haining, S. Sarkar, V. Kalia, S. Subramaniam, J. N. Blattman, D. L. Barber, R. Ahmed, Molecular signature of CD8<sup>+</sup> T cell exhaustion during chronic viral infection. *Immunity* **27**, 670–684 (2007). [Medline](#)  
[doi:10.1016/j.jimmuni.2007.09.006](#)
47. S. A. Fuertes Marraco, N. J. Neubert, G. Verdeil, D. E. Speiser, Inhibitory receptors beyond T cell exhaustion. *Front. Immunol.* **6**, 310 (2015). [Medline](#)  
[doi:10.3389/fimmu.2015.00310](#)
48. L. Baitsch, P. Baumgaertner, E. Devêvre, S. K. Raghav, A. Legat, L. Barba, S. Wieckowski, H. Bouzourene, B. Deplancke, P. Romero, N. Rufer, D. E. Speiser, Exhaustion of tumor-specific CD8<sup>+</sup> T cells in metastases from melanoma patients. *J. Clin. Invest.* **121**, 2350–2360 (2011). [Medline](#) [doi:10.1172/JCI46102](#)
49. G. J. Martinez, R. M. Pereira, T. Åijö, E. Y. Kim, F. Marangoni, M. E. Pipkin, S. Togher, V. Heissmeyer, Y. C. Zhang, S. Crotty, E. D. Lamperti, K. M. Ansel, T. R. Mempel, H. Lähdesmäki, P. G. Hogan, A. Rao, The transcription factor NFAT promotes exhaustion of activated CD8<sup>+</sup> T cells. *Immunity* **42**, 265–278 (2015). [Medline](#)  
[doi:10.1016/j.jimmuni.2015.01.006](#)
50. S. D. Blackburn, H. Shin, G. J. Freeman, E. J. Wherry, Selective expansion of a subset of exhausted CD8 T cells by αPD-L1 blockade. *Proc. Natl. Acad. Sci. U.S.A.* **105**, 15016–15021 (2008). [doi:10.1073/pnas.0801497105](#)
51. S. Picelli, Å. K. Björklund, O. R. Faridani, S. Sagasser, G. Winberg, R. Sandberg, Smart-seq2 for sensitive full-length transcriptome profiling in single cells. *Nat. Methods* **10**, 1096–1098 (2013). [Medline](#) [doi:10.1038/nmeth.2639](#)
52. J. J. Trombetta, D. Gennert, D. Lu, R. Satija, A. K. Shalek, A. Regev, Preparation of single-cell RNA-seq libraries for next generation sequencing. *Curr. Protoc. Mol. Biol.* **107**, 4.22.1–4.22.17 (2014). [Medline](#)
53. H. Li, R. Durbin, Fast and accurate short read alignment with Burrows-Wheeler transform. *Bioinformatics* **25**, 1754–1760 (2009). [Medline](#) [doi:10.1093/bioinformatics/btp324](#)
54. A. McKenna, M. Hanna, E. Banks, A. Sivachenko, K. Cibulskis, A. Kernytsky, K. Garimella, D. Altshuler, S. Gabriel, M. Daly, M. A. DePristo, The Genome Analysis Toolkit: A MapReduce framework for analyzing next-generation DNA sequencing data. *Genome Res.* **20**, 1297–1303 (2010). [Medline](#) [doi:10.1101/gr.107524.110](#)
55. M. F. Berger, M. S. Lawrence, F. Demichelis, Y. Drier, K. Cibulskis, A. Y. Sivachenko, A. Sboner, R. Esgueva, D. Pflueger, C. Sougnez, R. Onofrio, S. L. Carter, K. Park, L. Habegger, L. Ambrogio, T. Fennell, M. Parkin, G. Saksena, D. Voet, A. H. Ramos, T. J. Pugh, J. Wilkinson, S. Fisher, W. Winckler, S. Mahan, K. Ardlie, J. Baldwin, J. W. Simons, N. Kitabayashi, T. Y. MacDonald, P. W. Kantoff, L. Chin, S. B. Gabriel, M. B. Gerstein, T. R. Golub, M. Meyerson, A. Tewari, E. S. Lander, G. Getz, M. A. Rubin, L. A. Garraway, The genomic complexity of primary human prostate cancer. *Nature* **470**, 214–220 (2011). [Medline](#) [doi:10.1038/nature09744](#)

56. K. Cibulskis, M. S. Lawrence, S. L. Carter, A. Sivachenko, D. Jaffe, C. Sougnez, S. Gabriel, M. Meyerson, E. S. Lander, G. Getz, Sensitive detection of somatic point mutations in impure and heterogeneous cancer samples. *Nat. Biotechnol.* **31**, 213–219 (2013). [Medline](#) [doi:10.1038/nbt.2514](#)
57. C. T. Saunders, W. S. Wong, S. Swamy, J. Becq, L. J. Murray, R. K. Cheetham, Strelka: Accurate somatic small-variant calling from sequenced tumor–normal sample pairs. *Bioinformatics* **28**, 1811–1817 (2012). [Medline](#) [doi:10.1093/bioinformatics/bts271](#)
58. A. H. Ramos, L. Lichtenstein, M. Gupta, M. S. Lawrence, T. J. Pugh, G. Saksena, M. Meyerson, G. Getz, Oncotator: Cancer variant annotation tool. *Hum. Mutat.* **36**, E2423–E2429 (2015). [Medline](#) [doi:10.1002/humu.22771](#)
59. E. S. Venkatraman, A. B. Olshen, A faster circular binary segmentation algorithm for the analysis of array CGH data. *Bioinformatics* **23**, 657–663 (2007). [Medline](#) [doi:10.1093/bioinformatics/btl646](#)
60. B. Langmead, C. Trapnell, M. Pop, S. L. Salzberg, Ultrafast and memory-efficient alignment of short DNA sequences to the human genome. *Genome Biol.* **10**, R25 (2009). [Medline](#) [doi:10.1186/gb-2009-10-3-r25](#)
61. B. Li, C. N. Dewey, RSEM: Accurate transcript quantification from RNA-seq data with or without a reference genome. *BMC Bioinformatics* **12**, 323 (2011). [Medline](#) [doi:10.1186/1471-2105-12-323](#)
62. A. K. Shalek, R. Satija, J. Shuga, J. J. Trombetta, D. Gennert, D. Lu, P. Chen, R. S. Gertner, J. T. Gaublomme, N. Yosef, S. Schwartz, B. Fowler, S. Weaver, J. Wang, X. Wang, R. Ding, R. Raychowdhury, N. Friedman, N. Hacohen, H. Park, A. P. May, A. Regev, Single-cell RNA-seq reveals dynamic paracrine control of cellular variation. *Nature* **510**, 363–369 (2014). [Medline](#)
63. M. S. Kowalczyk, I. Tirosh, D. Heckl, T. N. Rao, A. Dixit, B. J. Haas, R. K. Schneider, A. J. Wagers, B. L. Ebert, A. Regev, Single-cell RNA-seq reveals changes in cell cycle and differentiation programs upon aging of hematopoietic stem cells. *Genome Res.* **25**, 1860–1872 (2015). [Medline](#) [doi:10.1101/gr.192237.115](#)
64. D. E. Campton, A. B. Ramirez, J. J. Nordberg, N. Drovetto, A. C. Clein, P. Varshavskaya, B. H. Friemel, S. Quarre, A. Breman, M. Dorschner, S. Blau, C. A. Blau, D. E. Sabath, J. L. Stilwell, E. P. Kaldjian, High-recovery visual identification and single-cell retrieval of circulating tumor cells for genomic analysis using a dual-technology platform integrated with automated immunofluorescence staining. *BMC Cancer* **15**, 360 (2015). [Medline](#) [doi:10.1186/s12885-015-1383-x](#)
65. I. Skaland, I. Øvestad, E. A. Janssen, J. Klos, K. H. Kjellevold, T. Helliesen, J. P. Baak, Comparing subjective and digital image analysis HER2/neu expression scores with conventional and modified FISH scores in breast cancer. *J. Clin. Pathol.* **61**, 68–71 (2008). [Medline](#) [doi:10.1136/jcp.2007.046763](#)
66. J. Konsti, M. Lundin, H. Joensuu, T. Lehtimäki, H. Sihto, K. Holli, T. Turpeenniemi-Hujanen, V. Kataja, L. Sailas, J. Isola, J. Lundin, Development and evaluation of a virtual microscopy application for automated assessment of Ki-67 expression in breast cancer. *BMC Clin. Pathol.* **11**, 3 (2011). [Medline](#) [doi:10.1186/1472-6890-11-3](#)

67. E. A. Eisenhauer, P. Therasse, J. Bogaerts, L. H. Schwartz, D. Sargent, R. Ford, J. Dancey, S. Arbuck, S. Gwyther, M. Mooney, L. Rubinstein, L. Shankar, L. Dodd, R. Kaplan, D. Lacombe, J. Verweij, New response evaluation criteria in solid tumours: Revised RECIST guideline (version 1.1). *Eur. J. Cancer* **45**, 228–247 (2009). [Medline](#)  
[doi:10.1016/j.ejca.2008.10.026](https://doi.org/10.1016/j.ejca.2008.10.026)